Máster en Física Avanzada

Especialidad Fotónica

Trabajo Fin de Máster

DYNAMICAL ANALYSIS OF ELECTRON TRANSPORT IN RF CAVITIES AND PHOTOMULTIPLIERS TUBES

Pablo Martín Luna

Tutor (1): Benito Gimeno Martínez
Tutor (2): Daniel González Iglesias

Curso académico 2020-2021

Contents

Resumen

El objetivo de este trabajo es el estudio de la dinámica de haces y corrientes de electrones en cavidades aceleradoras de radiofrecuencia (RF) y en tubos fotomultiplicadores.

Por una parte, los haces de electrones presentan una gran importancia histórica tanto en aplicaciones directas (televisiones, hornos de microondas, tratamiento del cáncer), como en la generación de radiación sincrotrón. La última generación de fuentes de rayos X muy brillantes se basa en los láseres de electrones libres (XFEL). No obstante, para producir los haces de electrones que emitirán dichos rayos X como radiación sincrotrón, se necesitan campos eléctricos de gran intensidad lo que produce que, debido a la emisión de electrones por efecto de emisión de campo en las paredes de los dispositivos, se generen las llamadas corrientes oscuras. Estas corrientes no solo perturban la dinámica de los haces de electrones, sino que incluso pueden producir un daño irreparable en el dispositivo mediante un fenómeno conocido como *RF breakdown*. Por este motivo, es de vital importancia estudiar la emisión de efecto de campo en los dispositivos aceleradores de alto gradiente y esta es la principal motivación de este trabajo.

Por otra parte, los tubos fotomultiplicadores son unos dispositivos que se usan en espectroscopía gamma desde hace más de 70 años, pero no hay prácticamente referencias donde se haya simulado su funcionamiento. Estos fotodetectores son bastante sensibles a los campos magnéticos externos. De hecho, incluso el campo magnético terrestre puede afectar a su funcionamiento. Por ello, se ha simulado un tubo fotomultiplicador con la finalidad de poder realizar en el futuro un diseño lo más adecuado posible para la realización de medidas en una habitación para el tratamiento con protonterapia.

Abstract

The aim of this work is the study of the dynamics of beams and electron currents in radio frequency (RF) accelerating cavities and in photomultiplier tubes.

Electron beams present a great historical importance both in direct applications (televisions, microwave ovens, cancer treatment) and in the generation of synchrotron radiation. The latest generation of very bright X-ray sources is based on free electron lasers (XFEL). However, to produce the electron beams that will emit the X-rays as synchrotron radiation, high intensity electric fields are needed, producing the emission of electrons (called dark currents) from the walls of the devices due to the effect of field emission. These currents can disturb the dynamics of the electron beams, but can also cause an irreparable damage to the device through a phenomenon known as RF breakdown. For this reason, it is of vital importance to study the field effect emission in high gradient accelerator devices and this is the main motivation for this work.

On the other hand, photomultiplier tubes are devices that have been used in gamma spectroscopy for more than 70 years, but there are practically no references where their operation has been simulated. These photodetectors are quite sensitive to external magnetic fields. In fact, even the Earth's magnetic field can affect its operation. Hence, a photomultiplier tube has been simulated in order to be able to make a design as suitable as possible in the future for carrying out measurements in a proton treatment room.

1 Introduction

Accelerator physics is a field in continuous expansion because particle beams have shown to be useful in multiple applications: fundamental particle physics, matter science, medical physics, Cathode Ray Tube (CRT) televisions, etc.

On the one hand, electron beams have found applications in many different areas since the discovery of the electron by Thomson in 1897. Low-energy (keV) electron beams have been used for domestic applications in CRT televisions or microwave ovens, while medium energy (MeV) electron beams are employed in hospitals for imaging and cancer treatment. High energy (GeV) electron beams are particularly important in science in order to investigate the properties of elementary particles, the nature of nuclear forces and the structure of matter. When accelerated electrons at relativistic speeds travel through a curved path, they emit electromagnetic radiation in the direction tangential to their path. This radiation is known as synchrotron radiation and is a very useful tool in other branches of physics, as well as in other fields of science such as molecular biology, medicine, geology or chemistry. The synchrotron radiation wavelengths ranges from X-rays to infrared light. X-radiation has penetrating capabilities which allows this radiation to make images of the body due to the different absorption coefficient of different tissues. But the main reason for the current research in X-rays is the fact that their wavelength, which is the magnitude that determines the smallest size one can study, is comparable to the atomic dimension. For this reason, X-rays are extremely useful to study the matter and they are in a continuous study in order to increase the brilliance[1] of this radiation.
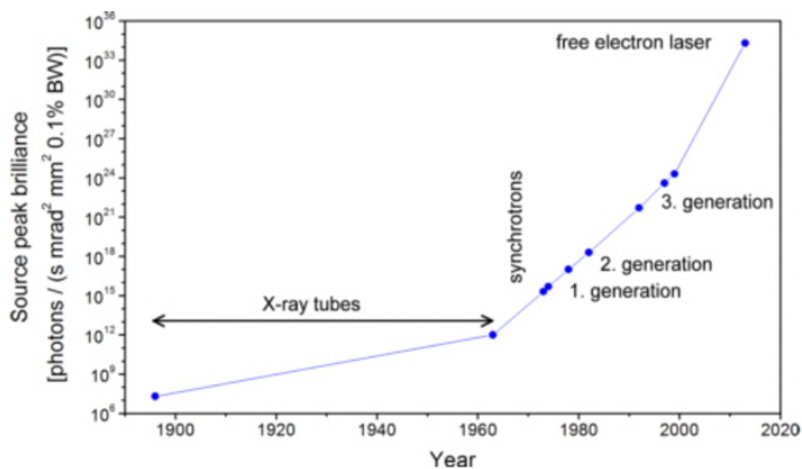

Figure 1: Evolution of average peak brightness of X-ray sources throughout history [1].

The progress made in brilliance since the discovery of X-rays by Röntgen in 1895 is shown in Figure 1. The first generation refers to machines for the collision of electron-positron beams designed to achieve the maximum collision ratios. The second generation of sources consisted of electron storage rings specifically designed as synchrotron radiation sources. The third generation was given by a big increase in brightness due to the use of undulators. The undulators are chains of magnetic dipoles placed together with alternating polarization. When electrons pass through this chain they undergo transverse oscillations, radiating in a narrow spectral range. However, the performance of these third

---

[1]The brilliance is defined as the photon flux per unit area, per unit solid angle, per unit spectral bandwidth, or, equivalently, the 6-D phase-space density of the photon beam.

generation devices cannot be improved much further because of fundamental limitations [2].

Consequently, the fourth generation of light sources is already under development. In this new generation the X-rays are generated in a single pass through the electron beam gain medium since it is not possible to build mirrors to reflect the X-rays for multiple passes through the medium because of the low reflectivities and potential mirror damage due to the high absorbed powers at the X-ray wavelength. It can be achieved using an X-ray Free Electron Laser (XFEL) which is based on a very long and carefully designed undulator in a high energy linear accelerator (linac). In this undulator the electrons amplify their neighbors spontaneous emission leading to efficient lasing in a single pass [3]. This process is known as Self Amplified Spontaneous Emission (SASE) and opens the way to a much shorter wavelength FEL because it does not require an optical cavity. The XFELs based on the SASE process will allow brightness peaks 100 million times greater than the existing synchrotron radiation sources in the third generation. Moreover, the radiation has full transverse coherence and the pulse length is reduced from the 100 ps time-domain down to the 100 fs time-domain [2].

There are already different XFEL facilities around the world, including those based on superconducting cavities such as European XFEL or LCLS-II, as well as those based on conductive cavities as SACLA or SwissFEL. In this sense, it is worth highlighting the European CompactLight project [4], whose goal was to bring together all the recent advances in the systems that make up an XFEL (such as electron injectors, linac accelerators and undulators) in order to achieve XFELs with a significant reduction in cost and size compared to current facilities, making them more affordable for small countries, regions and universities.

In an XFEL the electron source is typically a photoinjector that consists of an RF electron gun injector followed by accelerator structures. The electron bunch is generated by the illumination of the gun photocathode with short laser pulses. High gradients are required in order to mitigate space charge effects and provide high energies to electron beams in short distances, since particles just pass through cavities once. However, high gradients have a big drawback: electrons can be emitted from the cavity walls due to field effect. These electron currents are called dark currents and are emitted from microscopical protrusions where the electric field increases due to the lightning rod effect [5]. Furthermore, as a consequence of these high electric currents emitted from small tips, protrusions can be burnt by Joule effect, which can cause the emission of ions. These ion clouds can produce the reflection of the accelerators fields and even the device damage [6], [7]. This effect is known as RF breakdown and its evolution can be seen in Figure 2. For this reason, in this work, we will start by focusing on the numerical study of dark currents in RF electrons guns.

On the other hand, hadrons have been used in the Fermi National Accelerator Laboratory (Fermilab) or the Large Hadron Collider (LHC) in order to study fundamental particle physics allowing the discovery of new particles. One of the recent applications of hadrons is the hadron therapy in medicine. This therapy was first proposed by Wilson in 1946 [9], but it has not had a significant increase in the number of patients until the last decade. For example, the number of cancer patients treated worldwide with proton (C-ion) therapy has increased from $\sim$55 000 ($\sim$2000) per year in 2007 to $\sim$220 000 ($\sim$18 000) per year in 2019 [10]. Similarly, the number of hospitals with a hadron therapy facility increases annually: from $\sim$20 in 2007 to $\sim$100 in 2018 and $\sim$120 nowadays [11]. The essential advantage of hadron therapy over conventional radiotherapy (X-rays) is the
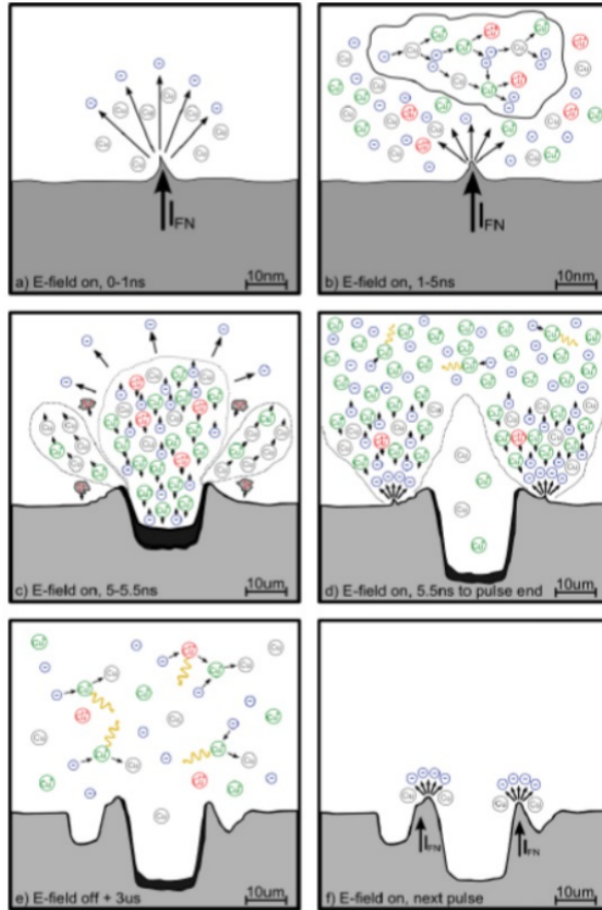
4

Figure 2: RF breakdown evolution [8].

existence of a peak in the energy deposition as a function of the depth of the tissue, as it can be seen in Figure 3. Therefore, most of the particle energy is lost at the end of the beam range[2], producing a sharp peak, known as the Bragg peak, just before the point where they are finally absorbed. Consequently, the dose can be concentrated in the tumor area, with little damage to the regions adjacent to the cancer. Thus, this therapy can be helpful in treatments which needs more accuracy, such as brain tumours.

Although there have been efforts from research institutions and industrial partners to reduce the size of hadron accelerators [12] as well as the overall price of facilities [13], the higher costs of hadron therapy with respect to conventional radiotherapy also limit its applicability [14]. Moreover, the inherent range uncertainty in the Bragg peak limits the potential of hadrons to conform the dose to the tumor since it forces the application of conservative safety margins during treatment planning, of up to ∼10 mm [15]. For this reason, it is important that hadron therapy facilities incorporates a system in order to verify in real-time where hadrons stop within the patient. There are different methods to achieve in vivo range verification, as positron emission tomography (PET) or prompt gamma-ray imaging (PGI). Prompt gamma-rays are photons generated when the nuclei that interact with the beam particles are de-excited. An example of a prompt gamma spectrum is shown in Figure 4. We can see some prominent lines due to the nuclear reactions with highest probability.

---

[2]The range of a charged particle is defined as the distance beyond which no such particles can penetrate. It depends on the beam energy and the target composition.
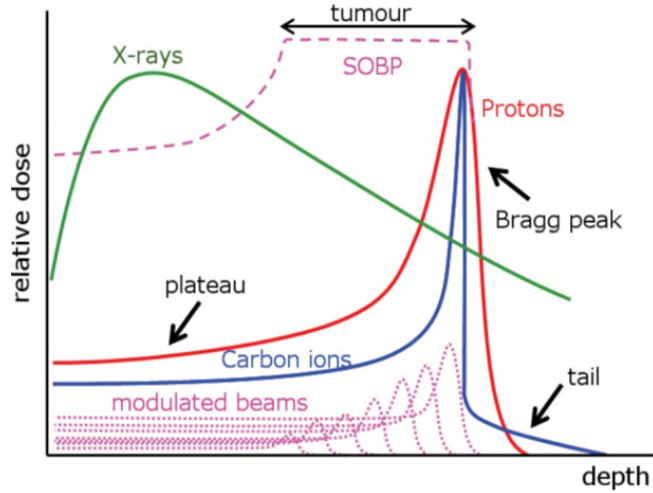
Figure 3: Relative dose as a function of depth for different types of radiation [8].
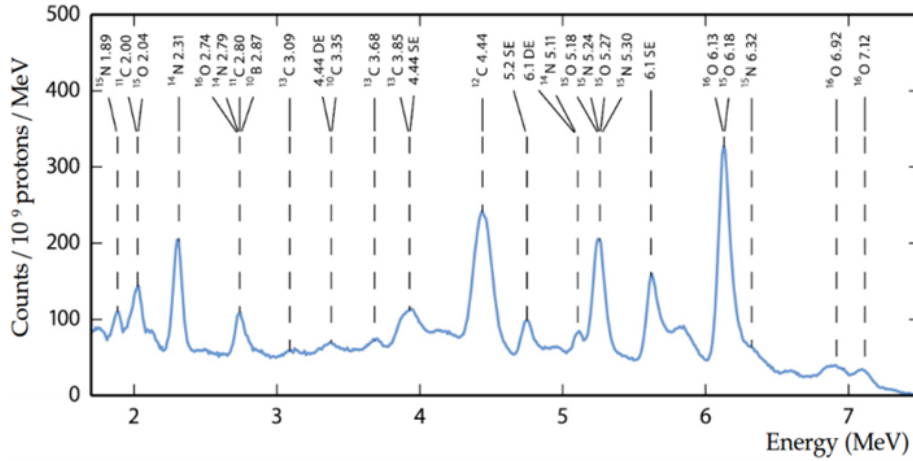

Figure 4: Prompt gamma energy spectrum measured from a water target irradiated with a proton beam. The nuclei responsible for the different lines are indicated [16].

It can be seen that the number of prompt gamma-rays detected per proton depends on the beam range [17]. Thus, exploiting the aforementioned dependence a compact and affordable method for proton range verification based on coaxial prompt gamma-ray has been proposed in 2020 [18]. Figure 5 shows the proposed detection setup. The prompt gamma-rays are detected by a scintillator crystal of $LaBr_3$ coupled to a photodetector. Although both silicon photomultipliers (SiPMs) [19] and photomultiplier tubes (PMTs) [20] have been used in prompt gamma spectroscopy as photodetectors, a PMT has been chosen in this setup in order to avoid the main disadvantages of SiPMs: a very fine temperature and bias voltage control [21]. However, PMTs are sensitive to magnetic fields [21] which are present in the treatment room since the gantry[3] beamline uses dipole and quadrupole magnets with magnetic fields of a few T [22], [23]. For this reason, we are going to simulate the operation of a PMT in order to study the dependence with the magnetic field with the future goal of finding the best PMT design for the prompt gamma-ray spectroscopy in a proton treatment room.

---

[3]The gantry is a large circular component, which contains the treatment delivery system and can rotate 360° around a patient to ensure the best beam angle for treatment.
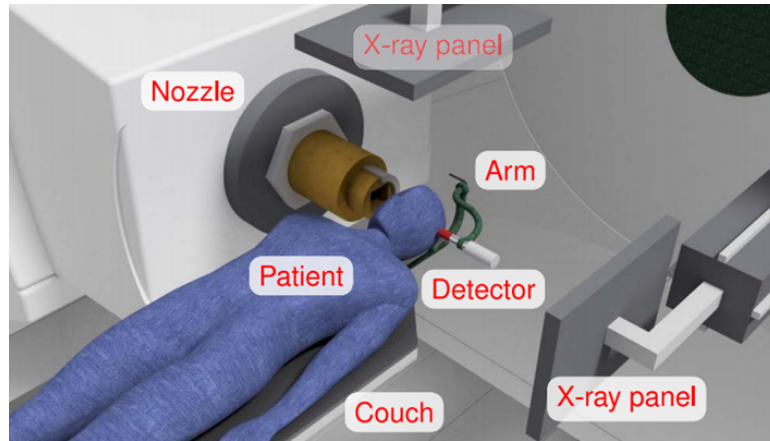
Figure 5: 3-D model of a detection setup in a proton treatment room. The beam incidence angle is horizontal and the scintillator detector (red) is coupled to a PMT. This detector is placed behind the treated area and coaxial to the beam, and is mounted on a rotating arm (green) attached to the patient couch. The X-ray panels can be used for measuring the detector position relative to the patient without interfering the treatment [18].

This master thesis is organized as follows. In Section 2 the emission from metal surfaces and the secondary electron emission are described. Moreover, the operation of an RF electron gun injector and a PMT is briefly explained and some considerations in the numerical solution of the electron dynamics are introduced. Next, in Section 3 the simulation codes that we have programmed and the corresponding results are presented and discussed. Finally, in Section 4, the main conclusions of these studies are outlined.

2 Theoretical framework

2.1 Electron emission from metal surfaces

Electrons can be emitted from a metal surface because of high temperatures (thermionic emission) or high electric fields (Fowler-Nordheim field emission).

On the one hand, in the 1910s, in the context of the difficulties of Drude's theory and its relation to the specific heat of metals, the works of Richardson [24], Schottky [25] and von Laue [26] allowed to obtain the Richardson-Schottky equation for the thermionic emission

$$J = AT^2 \mathrm{e}^{-\frac{\phi}{kT}}, \tag{1}$$

where J is the current density, T is the temperature, ϕ is the work function of the metal, k is the Boltzmann's constant and $A = 1.2 \times 10^6$ A/m^2 K^2 is a universal constant which was obtained by Dushman [27] applying the quantum theory (although Dushman obtained an error by a factor 2 in the numerical value because he did not take into account the electron spin).

On the other hand, in 1928, following the Sommerfeld's electron theory of metals, Fowler and Nordheim [28], [29] explained the field emission using the quantum tunneling through a potential barrier. The field emission can be calculated by the expression

$$J = \frac{1.54 \times 10^{-6} \times 10^{4.52\phi^{-0.5}} (E)^2}{\phi} \exp\left[-\frac{6.53 \times 10^9 \phi^{1.5}}{E}\right] \qquad \left[\mathrm{A/m^2}\right], \tag{2}$$

where J is the current density, ϕ is the work function (in eV) and E is the surface electric field amplitude (in V/m).

In 1956, Murphy and Good [30] unified thermionic and field emission theories obtaining a general expression for the electric current in terms of the electric field E, the temperature T and the work function ϕ.

The assumed effective potential energy $V(x)$ of an electron near the metal surface is (see Figure 6)

$$V(x) = \begin{cases} -W_a & x < 0, \\ -eEx - \frac{e^2}{16\pi\varepsilon_0 x} & x > 0, \end{cases} \tag{3}$$

where W_a is the electron energy in the metal, $e = 1.602 \times 10^{-19}$ C is the elementary charge, E is the electric field, ε_0 is the vacuum permittivity and x is the normal coordinate to the metallic surface. The term $-\frac{e^2}{16\pi\varepsilon_0 x}$ is the contribution of the interaction of the emitted electron with its image charge.
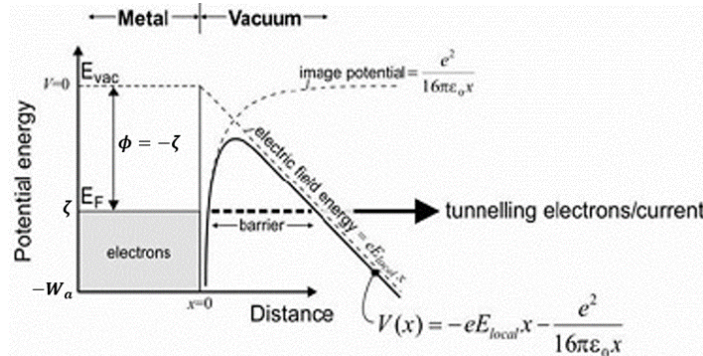

Figure 6: Potential energy of an electron near the metal surface [31].

If we assume that the conduction electrons in the metal form a gas which obeys the Fermi-Dirac statistics, the number of electrons inside a volume v with momenta in the range $dp_x dp_y dp_z$ is given by (the 2 appears because of the electron spin)

$$dn = \frac{2v}{h^3} \frac{dp_x dp_y dp_z}{e^{(\mathcal{E}-\zeta)/kT} + 1}, \tag{4}$$

where h is the Planck's constant, $\mathcal{E}$ is the total energy of the electron and ζ is the Fermi's energy. If we define the x-part of the energy of the electron $W = \mathcal{E} - \frac{p_y^2}{2m} - \frac{p_z^2}{2m} = \frac{p_x^2}{2m} + V(x)$, with m the electron mass, the flux of electrons with x-energy within dW incident on the surface is:

$$N(W, T, \zeta)dW = \frac{2}{h^3}dW \int_{-\infty}^{\infty}\int_{-\infty}^{\infty} \frac{dp_y dp_z}{e^{\frac{W-\zeta}{kT} + \frac{p_y^2 + p_z^2}{2mkT}} + 1} = \frac{4\pi mkT}{h^3} \ln\left(1 + e^{-\frac{W-\zeta}{kT}}\right), \tag{5}$$

where the double integral is easily solved introducing polar coordinates [32]. Otherwise, in the Wentzel, Kramers and Brillouin (WKB) approximation, the transmission coefficient (i.e. the probability that an electron incident with an x-energy W on the surface potential barrier emerges from the metal into the externally applied electric field) is [32]:

$$D(E, W) = \exp\left[-\int_{x_1}^{x_2} \sqrt{\frac{8m}{\hbar^2}[V(x) - W]}dx\right], \tag{6}$$

where $\hbar = h/(2\pi)$, and x_1 and x_2 are the zeros of the radicand, chosen so that $x_1 < x_2$.

Thus, the electric current that is emitted from a metal surface can be expressed in general as

$$J(E, T, \zeta) = e\int_{-W_a}^{\infty} D(E, W)N(T, \zeta, W)dW. \tag{7}$$

Murphy and Good [30] showed that this expression can be approximated to the Richardson-Schottky equation (1) in high temperature and low electric field situations; and to the Fowler-Nordheim equation (2) for low temperatures and high electric fields (see mathematical details in [32] or [5]). Moreover, they demonstrated that exists an intermediate region between these two approximations, as it can be seen in Figure 7.
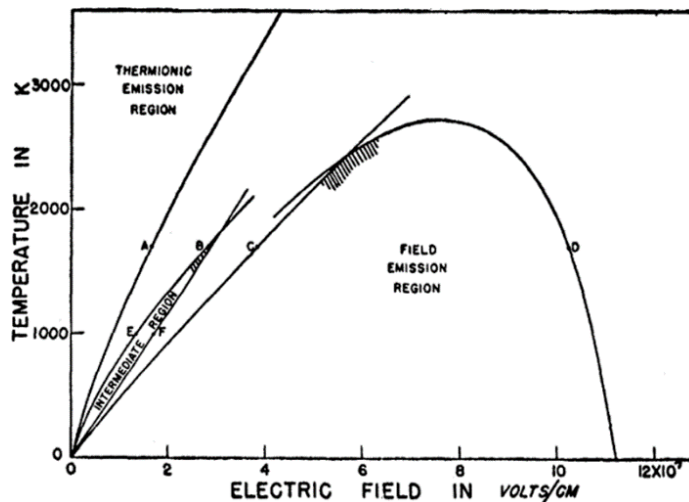

Figure 7: The three emission regions for $\phi = 4.5$ eV [30].

However, the metal surface in an accelerator cavity is not perfectly clean and flat and has microscopic protrusions where the amplitude of the surface electric field increases because of the lightning rod effect. These protrusions can be produced by metallic surface roughness (e.g microprotrusions, scratches), metallic dust, grain boundaries, molten craters after breakdown, absorbed gas, etc. [5]. This effect can be modeled with a field enhancement factor β which depends on the geometry of the protrusion and the material. Therefore, finally, the Fowler-Nordheim equation is written as

$$J_{\text{FN}}(E) = \frac{1.54 \times 10^{-6} \times 10^{4.52\phi^{-0.5}}(\beta E)^2}{\phi} \exp\left[-\frac{6.53 \times 10^9 \phi^{1.5}}{\beta E}\right] \quad \left[\text{A/m}^2\right], \quad (8)$$

where β has typical values of 6 to 100 [7]. In Figure 8, we have plotted the Fowler-Nordheim current density as a function of the product βE for different values of the work function.
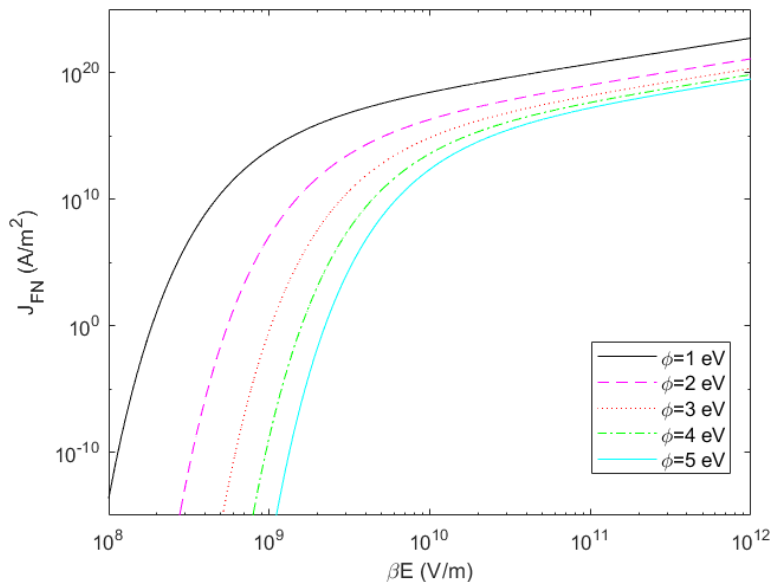

Figure 8: Fowler-Nordheim current dependence on electric field for different work functions.

As it is expected, the field emission increases if the work function decreases and the electric field increases. But the most important is that Fowler-Nordheim has an extreme non-linear dependence on the electric field since it changes 25 orders of magnitude with an increase of electric field 10 times larger. Hence, really small changes in the electric field amplitude can produce huge variations in the electron emission. As a consequence, electron field emission will accumulate in those spots where electric field is higher and these emitters can experience high temperature increases due to the Joule effect. This fact makes that the protrusions can be burnt, emitting metallic atoms in the process, which can cause RF breakdown in high gradient accelerator cavities (typically fabricated in copper).

2.2 Secondary electron emission

Secondary electron emission is the phenomenon where electrons are emitted from a surface induced by the impact of primary incident electrons with sufficient energy. This process is characterized by the total Secondary Electron Yield (SEY) coefficient, δ, which is the average number of electrons emitted per incident one:

$$\delta = \frac{\text{mean number of secondary electrons released}}{\text{1 impacting electron}}. \tag{9}$$

When an electron impacts on a surface, it can be absorbed, elastically or inelastically backscattered, or a number of true secondary electrons may be generated. Elastically backscattered electrons do not penetrate into the material and are released with the same energy and departure angle of impact, whereas inelastically backscattered electrons penetrate in the surface and are released with the same departure angle, but with a lower energy because of the interaction with the material. The other kind of emitted electrons interacts in a more complicated way with the material releasing more electrons if $\delta > 1$ or absorbing electrons if $\delta < 1$. These electrons are emitted with an energy and an angle which do not depend on the energy and impact angle of the primary electron (although the energy conservation principle implies that the total kinetic energy of all the output electrons must be equal or less than the primary electron). Figure 9 shows the three kinds of emitted electrons.
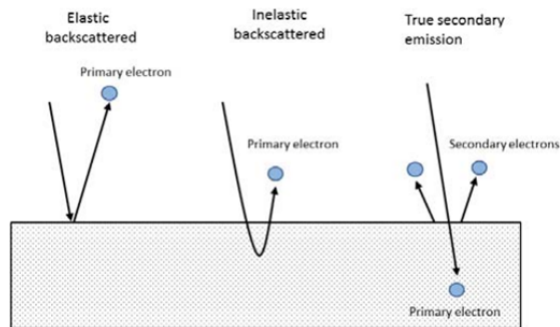

Figure 9: Scheme of the different kinds (elastically or inelastically backscattered and true secondary emission) of electron interaction with matter [33].

Given a certain material, the SEY coefficient depends only on the primary kinetic energy and the incidence angle of the impacting electron. The SEY curve has a common shape for all materials and an example is shown in Figure 10. At very low impact energies $E < E_0 \sim 10$ eV, electrons are mainly elastically backscattered, which implies that the value of the SEY curve is lower than 1; E_0 is an energy related to the work function of the material. Then, for $E_0 < E < E_1$, it is observed an absorption process, $\delta < 1$, but the SEY increases monotonically. However, for higher values of the energy, the true secondary emission is activated and becomes the main SEY contribution. We can see that there is an energy interval $E_1 < E < E_2$ in which the SEY value is greater than 1. The minimum and maximum energies of this interval are called the first cross-over point E_1 and the second cross-over point E_2, respectively. The maximum value of the SEY for normal incidence is defined as $\delta_{\max}$, and it is reached when the impacting energy is $E_{\max}$. For higher energies than E_2 the SEY drops monotonically, and inelastically backscattered electrons are predominant. Furthermore, the SEY value increases as the incidence angle (measured from the normal to the surface) does.
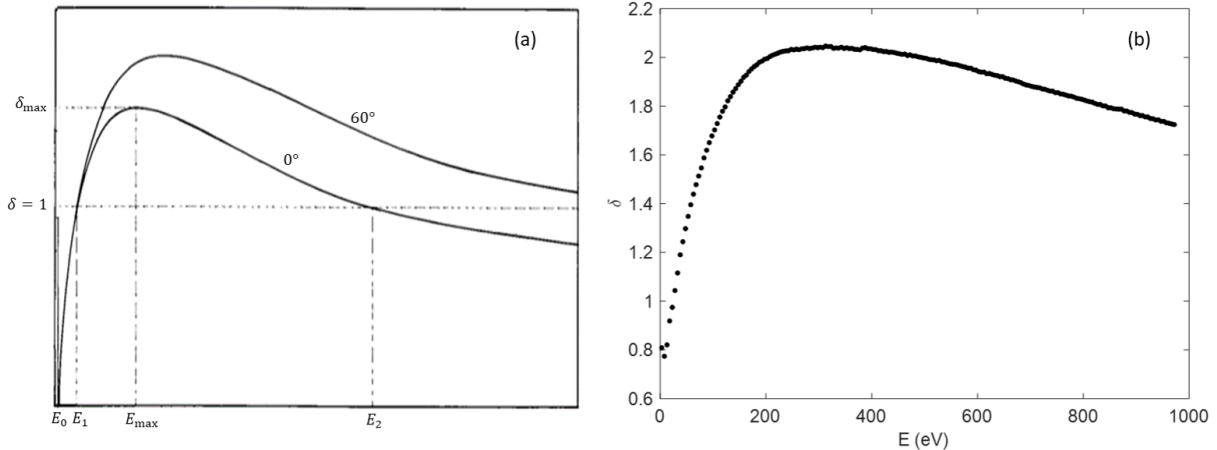
Figure 10: (a) Typical SEY curve as a function of the incident kinetic energy E for different incidence angles. Adapted from [34]. (b) Experimental silver SEY curve measured at the ESA-VSC High Power Space Materials Laboratory (courtesy of D. González-Iglesias).

There are several empirical and theoretical models to characterize the SEY curve. We are going to describe the modified Vaughan's model and the Furman and Pivi model.

2.2.1 Modified Vaughan's model

This model gives an empirical expression for the total SEY curve and was presented by C. Vicente et al [35] in 2005 as a modification of the model presented by Vaughan [34] in 1989. In this model, the SEY curve $\delta(E, \theta)$ as a function of the impacting electron kinetic energy E and the incident angle θ respect to the surface normal is given by the following expressions

$$\delta(E,\theta) = \begin{cases} \delta_{\text{low}} & \text{for} & v < 0, \\ \delta_{\max}(\theta)\left(ve^{1-v}\right)^k & \text{for} & 0 \leq v \leq 3.6, \\ \delta_{\max}(\theta)\frac{1.125}{v^{0.35}} & \text{for} & v \geq 3.6, \end{cases} \tag{10}$$

$$v = \frac{E - E_0}{E_{\max}(\theta) - E_0}, \tag{11}$$

$$\delta_{\max}(\theta) = \delta_{\max}\left(1 + k_\delta \theta^2 / 2\pi\right), \qquad E_{\max}(\theta) = E_{\max}\left(1 + k_E \theta^2 / 2\pi\right), \tag{12}$$

where $\delta_{\text{low}} \in [0, 1]$ is the SEY value at low impacting energies (typically close to the unity because at these energies electrons are mainly reflected on the surface), E_0 is a parameter related to the work function, k_δ and k_E are factors related to the roughness of the surface (normally taken equal to 1), $\delta_{\max}$ is the maximum SEY value and $E_{\max}$ is the energy at which $\delta_{\max}$ is given. Furthermore, k is a parameter that can have a smooth variation with v, but typically is chosen as [34]

$$k = \begin{cases} k_1 & \text{for } v \leq 1, \\ k_2 & \text{for } v > 1, \end{cases} \qquad k_i = \ln \delta_{\max} / \left(v_i - \ln v_i - 1\right) \quad (i = 1, 2), \tag{13}$$

where v_1 and v_2 are calculated substituting the first E_1 and second E_2 crossover, respectively, in equation (11) (note that the discontinuity of k is not a problem because $\left(ve^{1-v}\right)^k$ is insensitive to k at $v = 1$ and that the definition of k_i enforces that $\delta = 1$ in the first and second crossover).

Therefore, according to the previous expressions, the main input parameters needed for this SEY model are δ_{low}, δ_{max}, E_{max}, E_0, E_1 and E_2, which can be extracted from the experimental measurement of the SEY coefficient. Figure 11 shows a typical SEY curve given by the modified Vaughan's model for normal incidence of the electron.
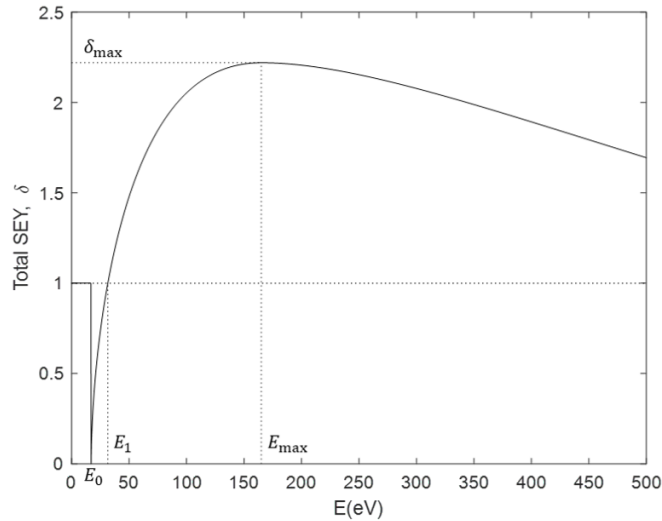

Figure 11: SEY curve at normal incidence for the modified Vaughan's model with parameters: $\delta_{\text{low}} = 1, \delta_{\text{max}} = 2.22, E_{\text{max}} = 165$ eV, $E_0 = 17$ eV, $E_1 = 30$ eV ($k_1 = 0.62$) and $E_2 = 2400$ eV ($k_2 = 0.25$), which are typical values for silver [35].

2.2.2 Furman and Pivi model

The SEY model formulated by Furman and Pivi [36], [37] is a probabilistic model which takes into account the contributions of the elastically backscattered, inelastically backscattered, and true secondary electrons to the total SEY coefficient. The contribution of the inelastically backscattered electrons is given by

$$\eta(E_p) = a(1 - bE_p) E_p^{\gamma} \exp\left(-\left(\frac{E_p}{E_b}\right)^{\mu}\right), \qquad E_b = c + dZ, \tag{14}$$

where Z is the atomic number of the surface material, a is a property of the material, usually in the range $[7 \times 10^{-3}, 10 \times 10^{-3}]$, $b = 3.0 \times 10^{-5}, c = 300, d = 175, \gamma = 0.50, \mu = 0.70$ and E_p is the primary electron kinetic energy in eV. The contribution from elastically backscattered electrons is modeled by

$$\varepsilon(E_p) = \frac{\varepsilon_1}{1 + \frac{E_p}{E_{e1}}} + \frac{\varepsilon_2}{1 + \frac{E_p}{E_{e2}}}, \tag{15}$$

where $\varepsilon_2 = 0.07$, $\varepsilon_1 = \varepsilon_0 - \varepsilon_2$, with ε_0 the value of the elastic contribution for $E_p = 0$, typically close to the unity, and $E_{e1} = g/\sqrt{Z}$, $E_{e2} = hZ^2, g = 50, h = 0.25$. Finally, the contribution due to true secondary electrons is given by

$$\delta(E_p) = \delta_{\text{max}} \frac{s \frac{E_p}{E_{\text{max}}}}{s - 1 + \left(\frac{E_p}{E_{\text{max}}}\right)^s}, \tag{16}$$

where $\delta_{\text{max}}, E_{\text{max}}$, and s are parameters of the material which can be extracted from the experimental measurement of the total SEY curve.

Moreover, the dependence on the angle θ with which the electron collides (measured from the normal of the surface) for the three previous expressions is given by

$$\delta\left(E_p, \theta\right) = \delta\left(E_p\right) \frac{k+1}{k+\cos\theta}, \qquad k = pZ + r, \tag{17}$$

$$\eta\left(E_p, \theta\right) = \eta\left(E_p\right)^{\cos\theta} C_1^{1-\cos\theta}, \qquad C_1 = \chi \frac{\eta\left(E_p\right)}{\eta\left(E_p\right) + \varepsilon\left(E_p\right)}, \tag{18}$$

$$\varepsilon\left(E_p, \theta\right) = \varepsilon\left(E_p\right)^{\cos\theta} C_1^{1-\cos\theta} C_2^{1-\cos\theta}, \qquad C_2 = \chi \frac{\varepsilon\left(E_p\right)}{\eta\left(E_p\right) + \varepsilon\left(E_p\right)}, \tag{19}$$

where $p = 0.0027$, $\chi = 0.89$, and note that $C_1 + C_2 = \chi$. For a clean surface, $r = 0$, but for rough surfaces, $2.5 < r < 10$; typically, $r = 5$. In Figure 12 it is shown an example with the different SEY contributions and the total SEY value, according to the Furman and Pivi model.
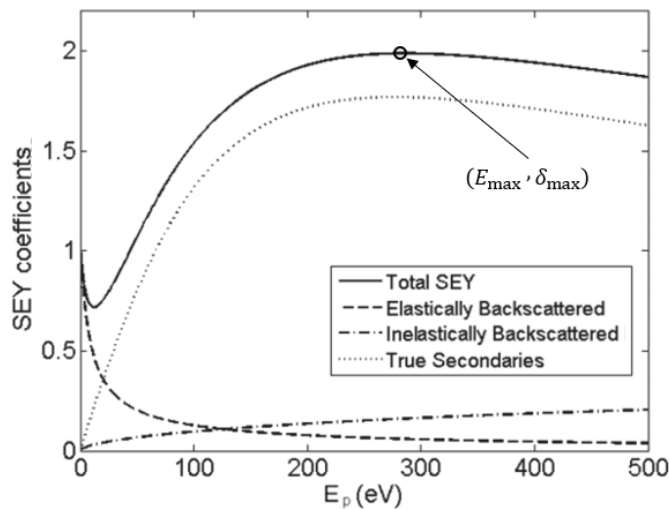

Figure 12: Typical Furman and Pivi SEY curve with the different kinds of emission contributions. Adapted from [33].

Thus, when an electron impacts on the metallic surface, the probability for each kind of emission is given by

$$P_e\left(E_p, \theta\right) = \varepsilon\left(E_p, \theta\right), \tag{20}$$

$$P_b\left(E_p, \theta\right) = \eta\left(E_p, \theta\right), \tag{21}$$

$$P_s\left(E_p, \theta\right) = 1 - P_e\left(E_p, \theta\right) - P_b\left(E_p, \theta\right). \tag{22}$$

The probabilities of a collision producing elastic or inelastically backscattered electrons are $P_e(E_p, \theta)$ and $P_b(E_p, \theta)$, respectively; and both types produce one emitted electron. However, whereas in the elastic case the incoming electron is perfectly reflected, in the inelastic case there is an energy loss between the incident and the departure electron. In the true secondary emission case, the probability is $P_s(E_p, \theta)$ and a random number of electrons per impacting electron are emitted following a Poisson distribution with an average number given by

$$\lambda\left(E_p, \theta\right) = \frac{\delta\left(E_p, \theta\right)}{1 - \varepsilon\left(E_p, \theta\right) - \eta\left(E_p, \theta\right)}. \tag{23}$$

14

2.3   RF electron gun injector

An RF gun is a photoinjector that is used as an electron beam source and allows to obtain high brightness electron beams. Although many different RF guns have been constructed and tested since they were introduced by Fraser et al. [38] in 1986, they have always the same structure (see a typical scheme in Figure 13). Firstly, the electron bunch is generated by illuminating the gun photocathode with short laser pulses. These electrons generated by photoelectric effect are rapidly accelerated by the RF electric field to reduce space charge effects. For this reason, high cathode gradients are required. The RF gun has a finite number of cells joined by irises to accelerate the electrons in each cell. To achieve it, the RF guns usually works in a π-mode and the cell length is $\lambda/2$, where λ is the free-space RF wavelength, except for the first cell which is shorter (typically about 0.6 times the length of the other cells) because the electrons are initially slower. The RF gun is usually powered via a coaxial coupler or a waveguide, components that are also employed to connect the RF gun to accelerator structures (with tenths or hundreds of cells) in order to obtain higher beam energies $\sim$100 MeV, as it can be seen in Figure 14. As the beam emittance[4] increases in the early stages of acceleration, the gun is typically surrounded by a solenoid magnet to reduce it [39].
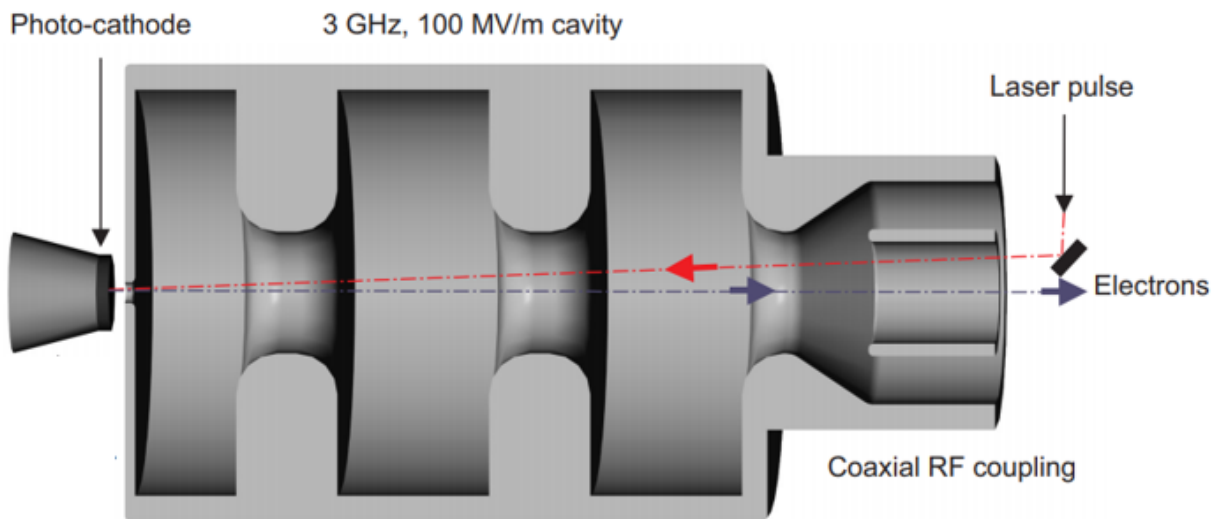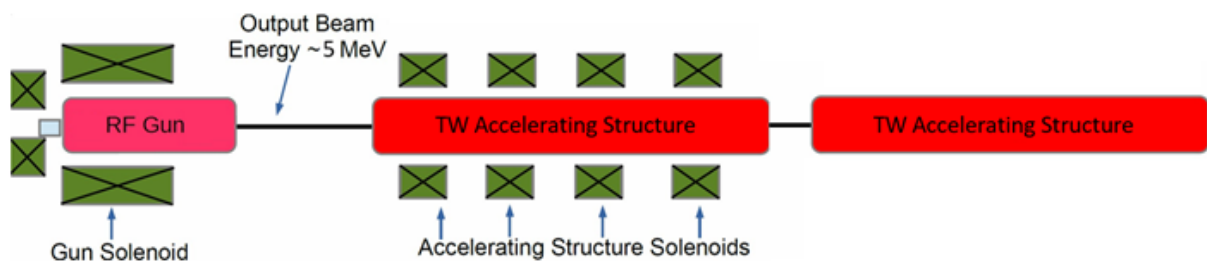

Figure 13: Scheme of a 2.5 cell RF gun [2].

Figure 14: RF photoinjector layout. After the RF gun, two travelling-wave (TW) accelerator structures are used to increase the beam energy to $\sim$100 MeV.

---

[4]Beam emittance is a measure for the average spread of particle coordinates in position-momentum phase space.

2.4 Photomultiplier tubes

A photomultiplier tube (PMT) is a non-thermionic vacuum tube that converts small light signals into a measurable electric current. A PMT consists of an input window to admit light, a photocathode, focusing electrodes (or grids), an electron multiplier and an anode grid. Figure 15 shows a typical scheme of a PMT.
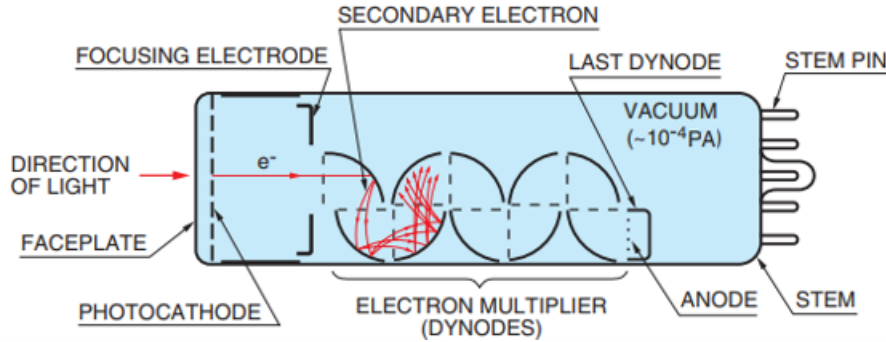

Figure 15: Construction of a PMT [40].

Typically, in gamma spectroscopy a scintillator crystal is placed just before the input window in order to convert energetic photons in optical photons [21]. Inorganic scintillator crystals are obtained adding impurities (activators) to a regular crystal lattice [41], [42]. Therefore, the energy band structure is modified creating intermediate energy states in the band gap around their sites and obtaining the diagram represented in Figure 16. Thus, an energetic photon that arrives to the scintillator crystal will produce an electron-hole pair exciting an electron from the valence to the conduction band. This electron will travel through the crystal producing multiple collisions before stopping and inducing the creation of more electron-hole pairs (and the emission of phonons). Finally, holes will quickly drift to an activator site and ionize it, and electrons will be captured in the ionized activators sites, producing an electron-hole recombination with the corresponding emission of an optical (scintillator) photon. In this way, it is achieved that an energetic photon is converted in optical photons (~ 3 eV) whose number is approximately proportional to the energy of the incident photon. Some examples of inorganic scintillator crystals are NaI(Tl), LYSO(Ce), GAGG(Ce) or LaBr$_3$(Ce).
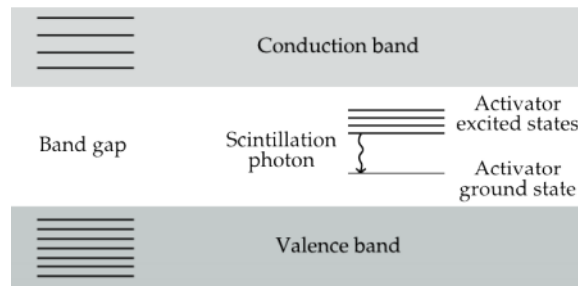

Figure 16: Diagram of an activated scintillator crystal band structure [41].

The photocathode is a semitransparent thin layer with a photoemissive material deposited on the inner surface of the window which absorbs the optical photons and emits photoelectrons because of the photoelectric effect. Bialkali materials (e.g. K$_2$CsSb, Rb$_2$CsSb) are normally used in photocathodes because they have a high quantum efficiency (number of photoelectrons emitted per number of incident photons) in the blue

region and low thermionic emission. The emitted photoelectrons are accelerated and fo-cused by the electrodes or grids onto the first dynode. The dynodes are covered with a layer of secondary emissive material (e.g. MgO, BeO, Cs_3Sb or Cu-BeO-Cs) in order to multiply the electrons when they impact on each dynode. The electron avalanche is finally collected by the anode where an electric current can be measured. To create the convenient electrostatic fields between dynodes to accelerate and focus the electrons is used a single high-voltage supply (>1000 V) and voltage dividers [42].

There are a variety of figures of merit in PMTs [42], [43]: single-electron resolution, signal-to-noise ratio, gain, linearity, response pulse timing, etc. depending on the appli-cation. We are going to define the gain, the electron transit time (ETT) and the transit time spread (TTS) which are the figures of merit that we have studied in this work. The gain of a PMT is the ratio of the anode current to the photocathode current, the ETT is the average interval time between the arrival of a light pulse at the photocathode and the collection of the corresponding current pulse at the anode (typical range 20-80 ns), and the TTS is the standard deviation of the pulse measured in the anode (sometimes the TTS is defined as the FWHM of the pulse, but we are going to use the previous definition for convenience). In Figure 17 we can see the response of a PMT to a short pulse of light on the photocathode that allows a better understanding of the definitions of the ETT and TTS.
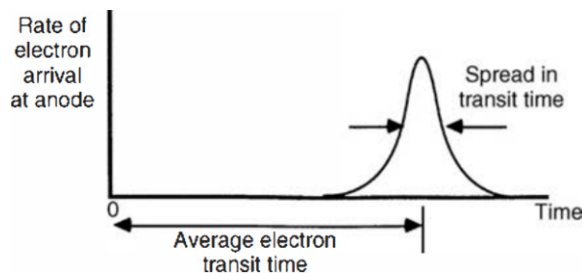

Figure 17: Scheme of a typical response of a PMT to a short pulse of light on the photocathode [42].

There are a lot of dynode types (see Figure 18) with different gains, time response and linearity depending on the structure, the voltages and the number of dynodes. For this reason, the optimum dynode type has to be selected according to the application.

2.5 Electron dynamics

2.5.1 The Boris method

In order to perform the numerical simulations we must use a method that allows us to solve the Lorentz force (a second-order differential equation system) numerically

$$\vec{F} = m\frac{d\vec{u}}{dt} = q(\vec{E} + \vec{v} \times \vec{B}), \tag{24}$$

where m is the rest mass and q the charge of the particle, $\vec{u} = \gamma\vec{v}$ is the relativistic moment normalized to the rest mass, $\gamma = \frac{1}{\sqrt{1-(v/c)^2}}$ is the Lorentz factor, $\vec{v} = \frac{d\vec{x}}{dt}$ is the velocity vector, $\vec{x}$ is the particle position, and $\vec{E}$ and $\vec{B}$ are the electric and magnetic field, respectively. Thus, we will use the Boris method [44], an explicit *Leap-frog* method that allows us to calculate the trajectories of the charged particle at certain times t_n,
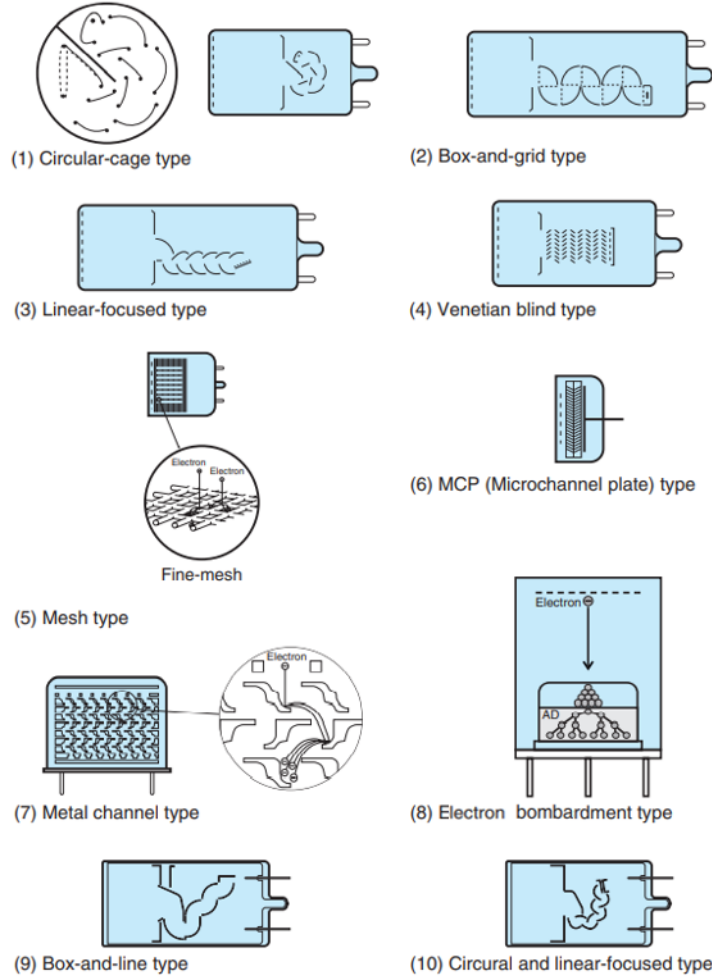
17

Figure 18: Types of dynodes used as electron multipliers in PMTs [40].

separated by a time interval Δt, using a discretization in time of the Lorentz force. Leap-frog methods are based on three simple steps [45]:

$$\vec{x}_{n+1/2} = \vec{x}_n + \frac{\vec{u}_n}{2\gamma_n}\Delta t, \tag{25}$$

$$\frac{\vec{u}_{n+1} - \vec{u}_n}{\Delta t} = \frac{q}{m}\left[\vec{E}\left(\vec{x}_{n+1/2}, t_{n+1/2}\right) + \vec{v} \times \vec{B}\left(\vec{x}_{n+1/2}, t_{n+1/2}\right)\right], \tag{26}$$

$$\vec{x}_{n+1} = \vec{x}_{n+1/2} + \frac{\vec{u}_{n+1}}{2\gamma_{n+1}}\Delta t, \tag{27}$$

where the subscript n refers to the value of the magnitude at the instant $t_n = t_0 + n\Delta t$. Note that the first and last steps consist of calculating the position of the particle assuming that it follows a rectilinear and uniform motion for a time $\Delta t/2$, while in the intermediate step the discretization of the Lorentz force is performed evaluating the electromagnetic fields in the position calculated in the first step, and assuming that the particle has an average velocity $\vec{v}$. Depending on how this average velocity is defined there are different numerical methods: Boris, Vay or Higuera-Cary [45]. In the Boris method its definition is

$$\vec{v} = \frac{\vec{u}_{n+1} + \vec{u}_n}{2\gamma_{n+1/2}}, \tag{28}$$

18

and has the property that, if we are in a case without electric field, the relativistic energy is conserved $E = m\gamma c^2$ (see appendix in [45]), as it is physically expected. If this definition is inserted in (26), we have that $\vec{u}_{n+1}$ can be calculated in a three-step process (two accelerations due to the electric field and an intermediate rotation due to the magnetic field):

$$\vec{u}^- = \vec{u}_n + \frac{q\Delta t}{2m}\vec{E}\left(\vec{x}_{n+1/2}, t_{n+1/2}\right), \tag{29}$$

$$\vec{u}^+ = \vec{u}^- + \left(\vec{u}^- + \left(\vec{u}^- \times \vec{k}\right)\right) \times \vec{s}, \tag{30}$$

$$\vec{u}_{n+1} = \vec{u}^+ + \frac{q\Delta t}{2m}\vec{E}\left(\vec{x}_{n+1/2}, t_{n+1/2}\right), \tag{31}$$

where we have defined $\vec{k} = \frac{q\Delta t}{2m\gamma^-}\vec{B}\left(\vec{x}_{n+1/2}, t_{n+1/2}\right), \vec{s} = \frac{2\vec{k}}{1+k^2}$ and $\gamma^- = \frac{1}{\sqrt{1+(u^-/c)^2}}$.

2.5.2 Effective electron model

In a typical simulation of Fowler-Nordheim field emission or secondary electron emission there are usually a very large number of electrons (with mass m and charge q), so calculation times can be very long. For this reason, it is common to use macroparticles (with mass $M = Nm$ and charge $Q = Nq$), which represent a number N of electrons. As the ratio between charge and mass is the same, the trajectory of these macroparticles will be the same as that of the individual electrons (neglecting the interactions between electrons). This approach is extremely useful and provides reliable results in many cases [35].

In the case of secondary electron emission, we can consider that the number of electrons $N_i(t)$ changes when the i-th macroparticle collides in a surface to $N_i(t+\Delta t)$ in the following way:

$$N_i(t + \Delta t) = N_i(t)\delta_{t,i}, \tag{32}$$

where $\delta_{t,i}$ is the SEY coefficient for that collision. Figure 19 shows an scheme of the charge and mass accumulation process for the effective electron model.
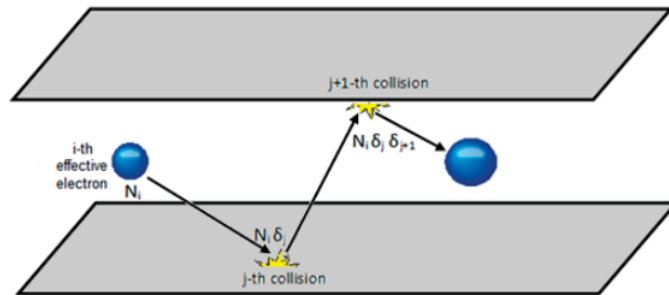

Figure 19: Scheme of the variation of N_i when the secondary electron emission occurs in the effective electron model [33].

3 Simulations

3.1 Dark currents

3.1.1 Simulation program

We are going to study the Fowler-Nordheim field emission (typically called *dark currents*) in two different RF electron gun injectors: an S-band 1.6 cell RF gun and an X-band 5.6 cell RF gun. As the RF gun is axisymmetric, the amplitude of the electric and magnetic field inside the device can be calculated with the 2D eigenmode solver SUPERFISH [46], which has the advantage of being much faster than 3D codes. The electromagnetic (EM) fields can be easily expressed in cylindrical coordinates (r, φ, z) as

$$\vec{E}(\vec{x}, t) = (E_r(r, z)\hat{r} + E_z(r, z)\hat{z}) \sin(\omega t),$$
$$\vec{B}(\vec{x}, t) = \mu_0 H_\varphi(r, z)\hat{\varphi} \cos(\omega t), \tag{33}$$

where μ_0 is the magnetic permeability of free space and $\omega = 2\pi f$ (f is the RF frequency). Nevertheless, SUPERFISH calculates the amplitude of EM fields in a grid in the plane (r, z). Therefore, we cannot directly use the expressions of the Boris method, since we do not know the analytical expression of the EM fields. Thus, in order to obtain the value of these fields at a general point (r, z), we are going to perform a bilinear interpolation [47], which is a 2D generalization of the usual linear interpolation. The general expression of this interpolation is

$$f(x, y) = (x_2 - x_1)^{-1} (y_2 - y_1)^{-1} \left[f(Q_{11})(x_2 - x)(y_2 - y) + \right.$$
$$\left. f(Q_{12})(x_2 - x)(y - y_1) + f(Q_{21})(x - x_1)(y_2 - y) + f(Q_{22})(x - x_1)(y - y_1) \right], \tag{34}$$

whose geometric interpretation can be seen in Figure 20, which indicates that the value of the function at an arbitrary point (x, y) is the mean of the value of the function f at the 4 closest points Q_{ij} (where we know its value) weighted by the area of the opposite rectangle to each vertex and normalized to the total area (sum of the surface of the four rectangles).
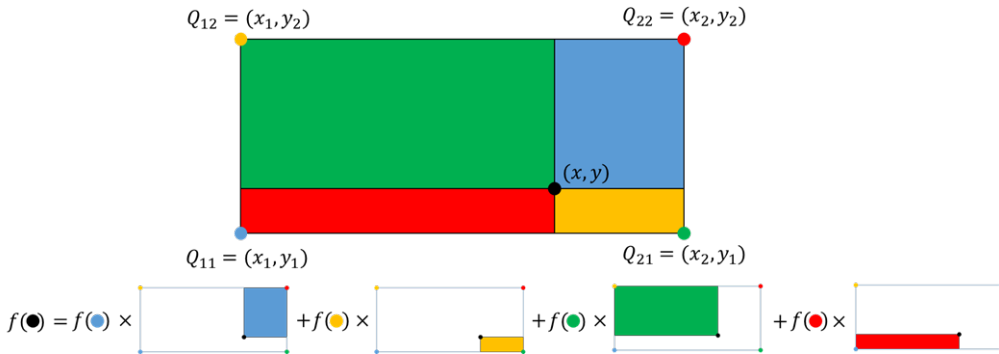

Figure 20: Geometric interpretation of bilinear interpolation.

We are going to consider a density $n = 10^5 - 10^6$ emitters/m^2 and circular tips with a radius of $r_{\text{em}} = 0.1 - 0.5$ μm which are typical values [7]. These emitters are randomly created in the surface of the device with a uniform distribution of probability (see Appendix A). Our simulation program numerically solves the electron relativistic dynamics using Boris method with a temporal step of $\Delta t = T_{\text{RF}}/300$ ($T_{\text{RF}} = 1/f$) and neglecting

space charge effect and secondary electron emission, unless otherwise specified. In each temporal step the Fowler-Nordheim current density, equation (2), is calculated and a macroparticle with a charge $Q = -J_{\text{FN}}\Delta t\,(\pi r_{\text{em}}^2)$ is emitted without initial kinetic energy (if $|Q| < 0.1e$, being e the elemental charge, the macroparticles are not considered in order to reduce the computing time). Furthermore, we will study the dark currents turning off the solenoid magnet that surrounds the RF electron gun injector to reduce the beam emittance since, in the future, it is intended to perform the measures of the dark currents without the solenoid.

3.1.2 1.6 cell RF electron gun injector

We are going to start simulating the dark current emission for an S-band 1.6 cell RF electron gun injector designed at INFN (Frascati-Roma, Italy) which operates at $f = 1/T_{\text{RF}} = 2856.3149$ MHz in the π-mode with a cathode gradient of 120 MV/m. The cross section of this RF gun, as well as the direction of the electric field is shown in Figure 21. It consists of a photocathode, a first cell with length 0.6 $\lambda/2$, where λ is the free-space RF wavelength, a second cell with length $\lambda/2$, and a circular waveguide. The cells are joined by means of elliptical irises instead of circular ones to reduce the peak iris electric field [48], which should diminish the dark current emission and thus the likelihood of RF breakdown.
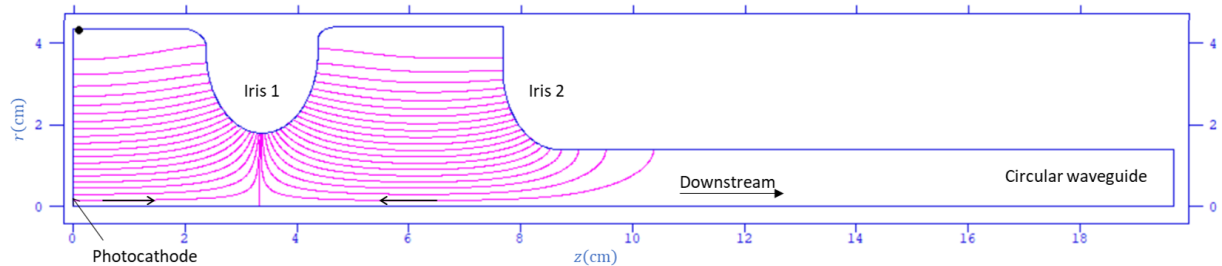

Figure 21: Cross section of the axial symmetric 1.6 cell RF gun with the circular waveguide. The field lines in the cavity are lines of constant rB_φ, which are parallel to the electric field.
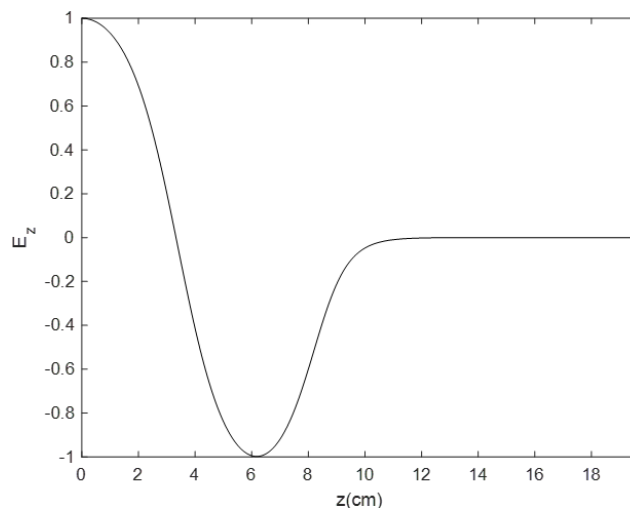

Figure 22: Electric field along the axis of the 1.6 cell RF gun, normalized to the maximum value at photocathode.

Figure 22 shows the amplitude of the electric field along the gun axis. As it is expected for the π-mode, the electric field is in phase opposition between cells. Otherwise, the surface electric field along the RF gun contour is shown in Figure 23. We can see that the surface electric field is higher at the center of the photocathode and at the irises. Therefore, the non-linear relation of the Fowler-Nordheim field emission, equation (2), with the electric field entails that electron emission from the surfaces are only relevant at those zones.
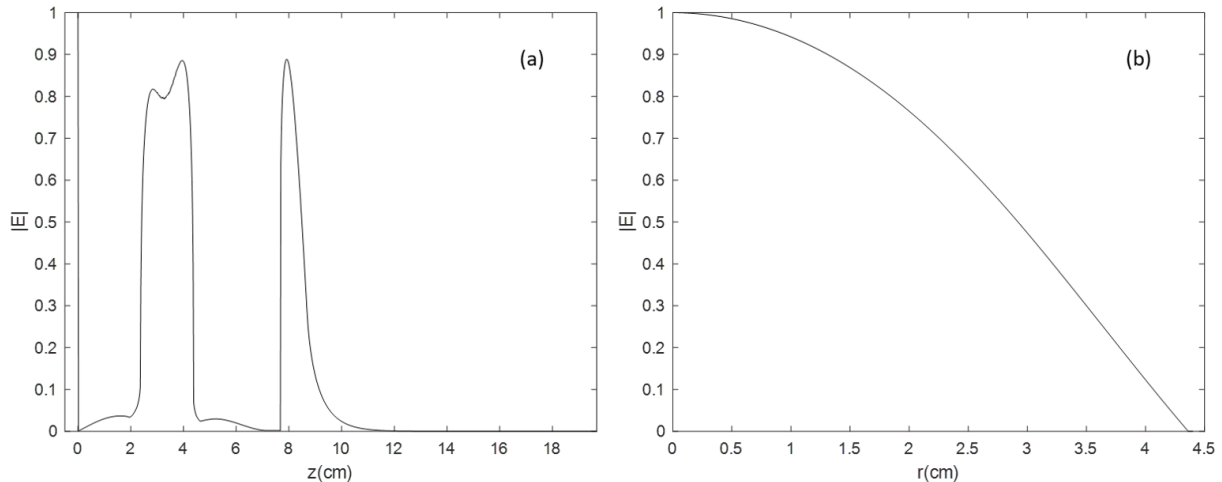

Figure 23: (a) Surface electric field as a function of the axial position. (b) Electric field at the photocathode surface as a function of the radial position. Values normalized to the maximum value at photocathode of the 1.6 cell RF gun.

We are going to use the parameters indicated in Table 1 to perform the simulations. The value of the work function corresponds to copper.

Table 1: Values of the field enhancement factor β, work function ϕ, density of emitters n and tip radius r_{em} used for the simulation of dark currents in the 1.6 cell RF gun.

β	$\phi(\text{eV})$	$n\,(\text{m}^{-2})$	$r_{em}(\mu\text{m})$
60	4.5	10^5	0.1

In Figure 24 we have plotted the positions of emitted macroparticles at different times. Due to the distribution of the electric field, dark currents are emitted periodically from the first iris at $t = T_{RF}/4$ and from the other iris and the photocathode at $t = 3T_{RF}/4$. Figure 25a shows the current emitted from photocathode and the irises as a function of time.

Approximately 93.3% of emitted macroparticles impact on the surface of the structure (mainly on the irises) and the majority have kinetic energies of $\sim$1 MeV, as it can be seen in Figure 25b and Figure 26a,b. In fact, the minimum value of the kinetic energy of electrons impacting on the metallic wall is $\sim$10 keV. Therefore, these electrons will mostly be absorbed because for kinetic energies greater than 1-2 keV the total Secondary Electron Yield (SEY) coefficient, which is the mean number of emitted electrons per incident electrons, is much smaller than one [34].

In addition, in Figure 25c we can see that the downstream electrons that arrive to the final of the circular waveguide represent 1.2% of the emitted electrons and they were
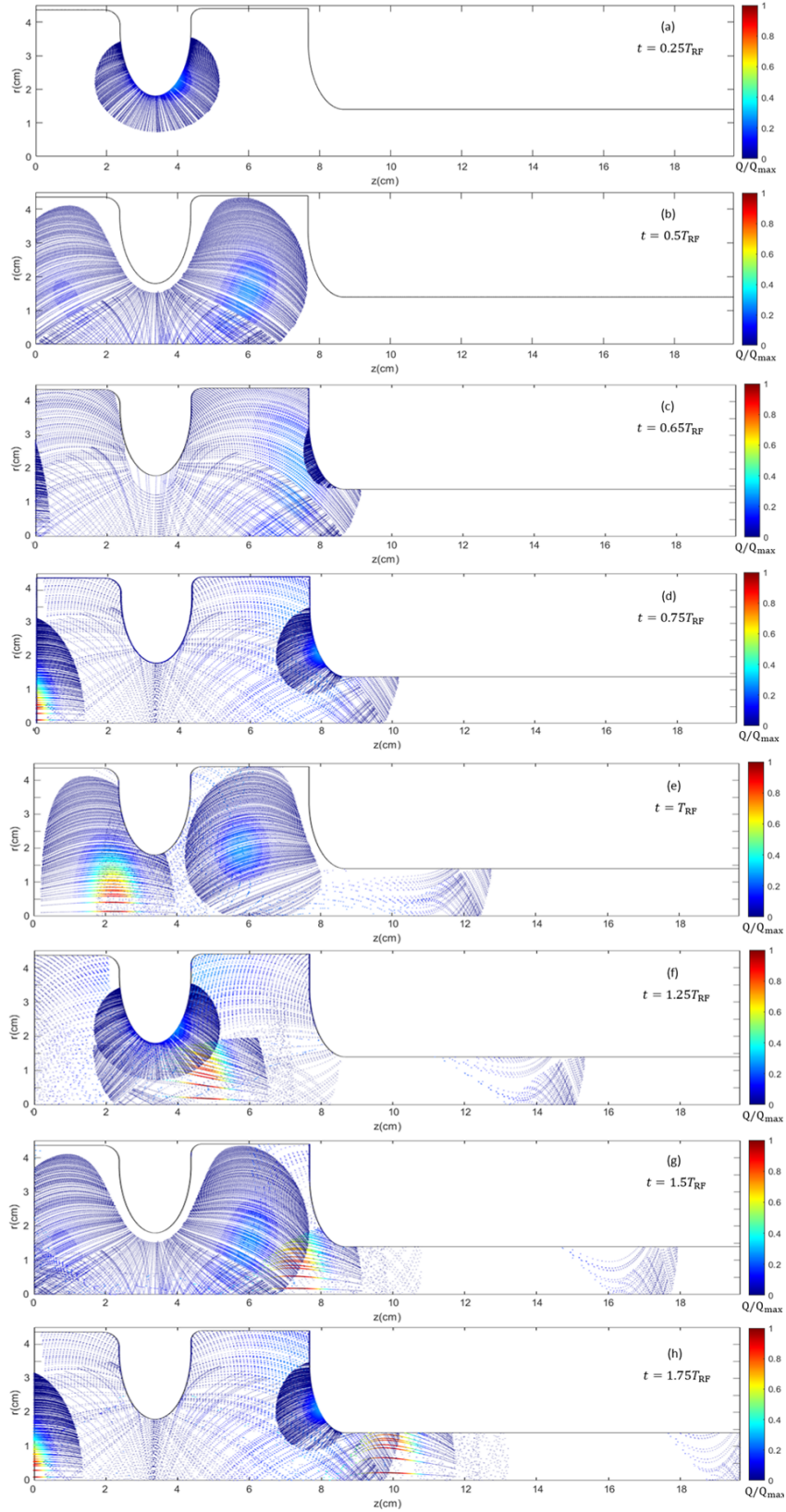
Figure 24: The dark current macroparticles positions (projected in the (r, z) plane) at the time instant (a) $t = 0.25T_{\mathrm{RF}}$, (b) $t = 0.5T_{\mathrm{RF}}$, (c) $t = 0.65T_{\mathrm{RF}}$, (d) $t = 0.75T_{\mathrm{RF}}$ (e) $t = T_{\mathrm{RF}}$, (f) $t = 1.25T_{\mathrm{RF}}$, (g) $t = 1.5T_{\mathrm{RF}}$ and (h) $t = 1.75T_{\mathrm{RF}}$. Color indicates the charge of the macroparticles normalised to the maximum macroparticle charge $Q_{\mathrm{max}} = -94626e$.

23

emitted mainly from the photocathode and the first iris. Moreover, electrons emitted from the photocathode arrive with higher kinetic energies (see Figure 26c) in bunches, whereas electrons emitted from the first iris arrive normally scattered with a kinetic energy of ~ 1.1 MeV or ~ 5 MeV.
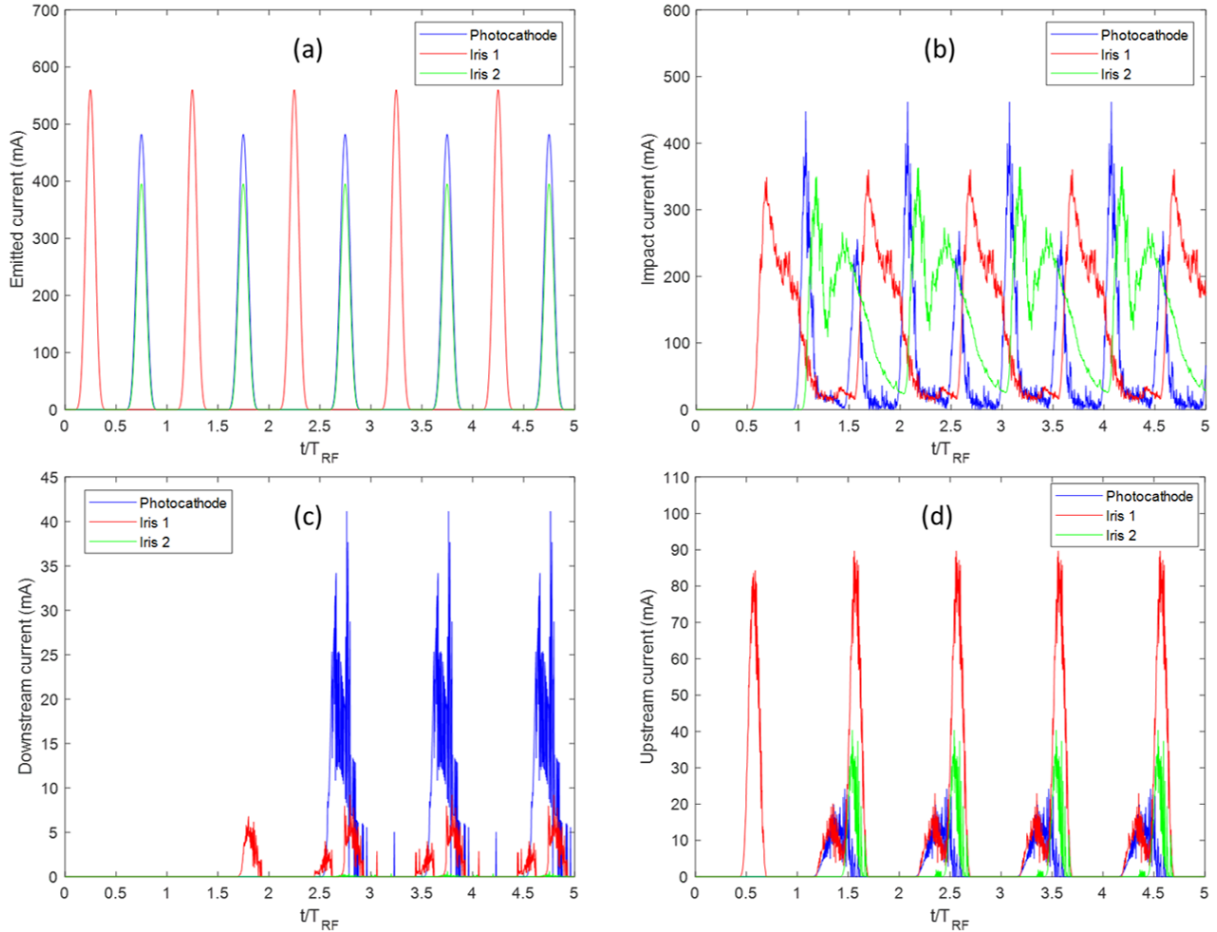

Figure 25: (a) Emitted dark current, (b) current that impacts on the surface of the structure, (c) downstream current that arrives to the final of the circular waveguide and (d) upstream current that arrives to the photocathode as a function of time.

Upstream electrons that arrive to the photocathode represent about the 5.5% of the emitted electrons. The kinetic energy spectrum of the electrons emitted from the first iris has two contributions (Figure 26d). The first peak between approximately 0 and 2 MeV corresponds to electrons that are emitted upstream and impact on the photocathode in the same period they were emitted. In other side, electrons with higher energies are initially accelerated downstream, but they are accelerated upstream before they arrive to the circular waveguide and finally impact on the photocathode in the next period (some of them do not arrive to the photocathode and are accelerated downstream again and explain the peak about 5 MeV in Figure 26c). Upstream electrons emitted from the second iris have a widespread kinetic energy spectrum, whereas some electrons emitted from the photocathode come back to the photocathode impacting with kinetic energies of ~ 1.1 MeV.
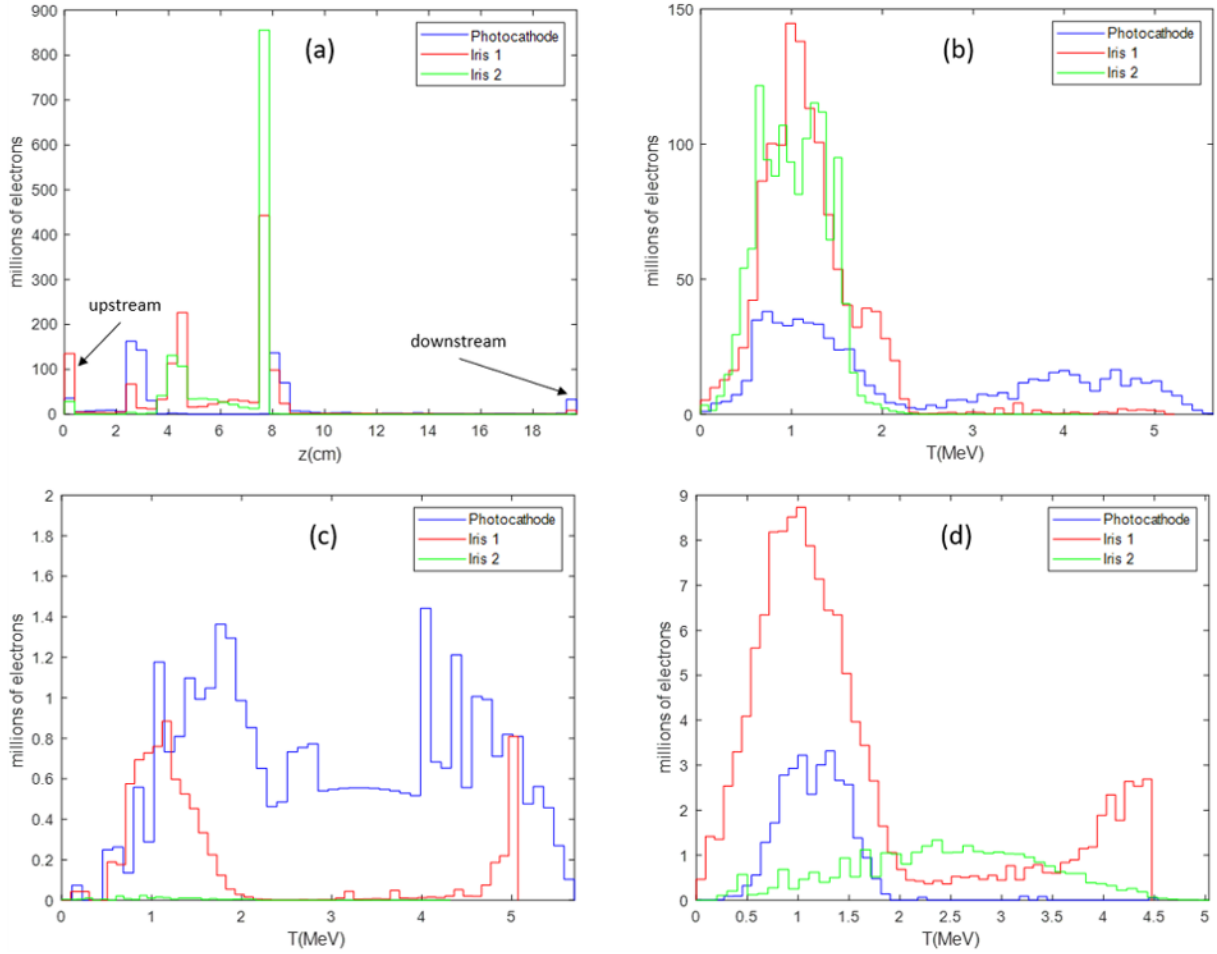
24

Figure 26: (a) Histogram of impact z-position, including upstream and downstream electrons. Kinetic energy spectra for (b) impact electrons, (c) downstream electrons and (d) upstream electrons after $5T_{RF}$.

Once the dynamics of the dark currents in the RF gun have been studied, we are going to focus on how to measure the downstream current using a Faraday cup. A Faraday cup is a metal cup that is used to measure the total charge of beams [49]. It consists of two conducting cylinders (see Figure 27) whose ratio between the diameters of the outer and inner cylinders is 2.3 to achieve a 50 Ω impedance matching [50]. The resulting current produced because of the electrons (or ions) that hit the inner cylinder can be measured and used to determine the number of charged particles hitting the cup. Thus, to increase the electrons that reach the inner cylinder, the Faraday cup is usually surrounded by a solenoid that generates a powerful magnetic field, since it allows the electrons to be focused on the axis of the solenoid [51]. Typically, a ferromagnetic material ($\mu_r \sim 250$) is placed surrounding the coil of the solenoid since it strongly increases the magnetic field allowing to obtain magnetic fields $\sim$1 T with the usual DC currents that feed the solenoid. Our proposed design of the solenoid is shown in Figure 28.

In this study we are going to do a preliminary study taking into account the secondary electron emission. Thus, we will use the Furman and Pivi model with $\delta_m = 2.22$, $E_m = 200$ eV and $s = 1.35$, which have been extracted from a fit to experimental measurements of the copper SEY curve, $\epsilon_0 = 1$ and $r = 0$ (we assume a clean surface).
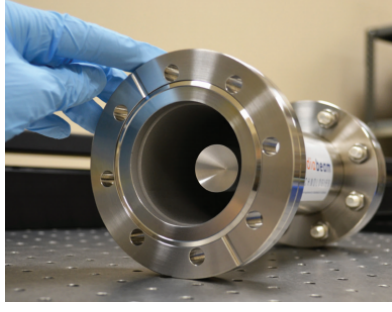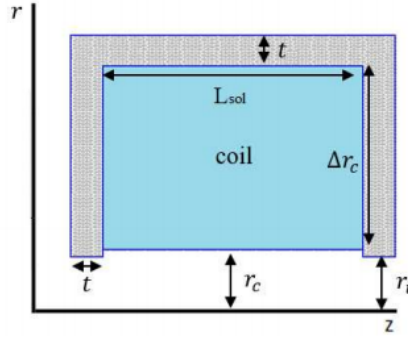
Figure 27: Photography of a Faraday cup [52].

Figure 28: Solenoid diagram consisting of a coil and a ferromagnetic material surrounded it with $\mu_r = 250$ (low carbon steel). Solenoid parameters: $r_c = 4$ cm, $\Delta r_c = 12$ cm, $t = 2$ cm, $r_i = 3.5$ cm, $z_{\text{sol}} = 20$ cm and $L_{\text{sol}} = 20$ cm.
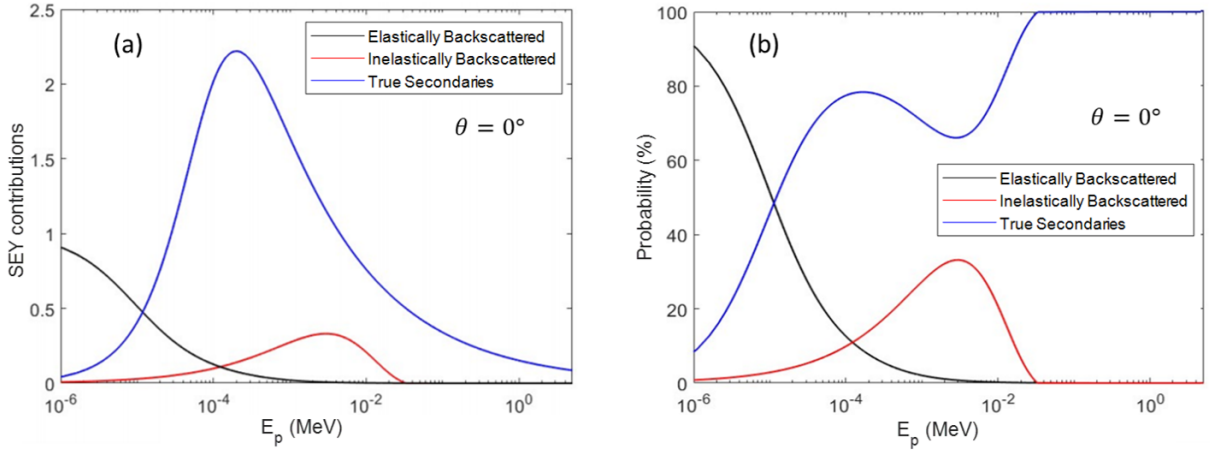

Figure 29: Elastic, inelastic and true secondary (a) contributions to SEY and (b) probabilities for copper in the energy range [0, 5 MeV] at normal incidence.

Figures 29 and 30 show the SEY and probability of the different kinds of emission contributions for normal incidence and $\theta = 82.5°$, respectively. We can see that the SEY increases with θ and the existence of an important difference at low energies: for normal incidence predominates the elastically backscattered electrons, whereas for oblique incidence predominates true secondary electrons. Furthermore, the SEY is much lower than one for energies greater than 1 MeV (which are the typical impact energies, see Figure 26). For this reason, secondary electron emission has been neglected in the previous study. However, inelastically backscattered and true secondary electron emission are
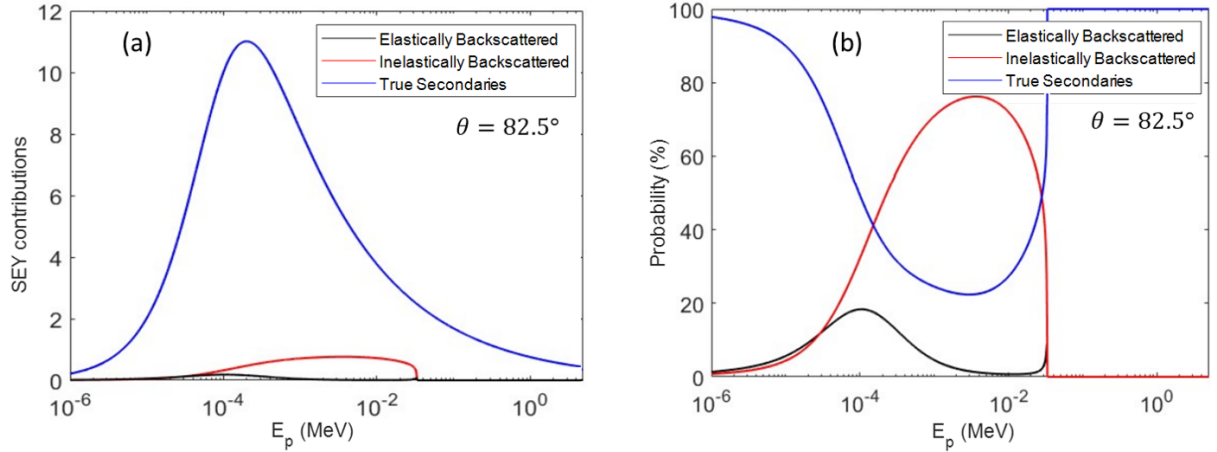
Figure 30: Elastic, inelastic and true secondary (a) contributions to SEY and (b) probabilities for copper in the energy range [0, 5 MeV] at oblique incidence with $\theta = 82.5°$.

typically emitted with kinetic energies of a few eV. As in the circular waveguide and the drift tube[5] the EM fields decrease considerably, these emitted electrons impact on the surface with kinetic energies of a few eV, energies where the secondary electron emission cannot be neglected. Consequently, we are going to consider the secondary electron emission from a distance of 9.8 cm to the photocathode, as it is indicated in Figure 32.

Thus, when an effective electron impacts on a surface, the probabilities for each kind of electron interaction with the surface are calculated with equations (20-22), and one of them is chosen generating a random number $u \in [0, 1]$, [33]:

$$u < P_e(E_p, \theta) \longrightarrow \text{ Elastic backscattered electron,}$$
$$P_e(E_p, \theta) \leq u < P_e(E_p, \theta) + P_b(E_p, \theta) \quad \longrightarrow \quad \text{Inelastic backscattered electron,}$$
$$u \geq P_e(E_p, \theta) + P_b(E_p, \theta) \quad \longrightarrow \quad \text{True secondary electron.}$$

As we explain in Section 2.2.2, in the elastic case, the incoming electron is perfectly reflected. In other cases we will follow J. de Lara et al. [37] to calculate the output energy. If there is an inelastic backscattering collision, the energy of the emitted electron will be calculated by the inverse cumulative probability function

$$G_b(u) = \alpha^{(-1/n_b)} \cdot (\arccos(1 - \beta \cdot u))^{(1/n_b)},$$
$$\beta = 1 - \cos(\alpha), \quad \alpha = \pi \cdot X_{cb}^{n_b}, \tag{35}$$

where n_b and X_{cb} are parameters of the material. Firstly, a random number $u \in [0, 1]$ is generated and the energy of the emitted electron is

$$E_b = E_p \cdot G_b(u), \tag{36}$$

where E_p is the primary electron kinetic energy. Otherwise, in the case of a true secondary emission collision, the number of emitted electron is calculated using the equation (23) and the number of the electrons of the effective electron is calculated with equation (32). Once this number has been obtained, the kinetic energy of the departure effective electron is computed as

$$E_{se} = E_p \cdot G_s(u). \tag{37}$$

---

[5]A drift tube is a conducting enclosure, usually cylindrical, that connects the circular waveguide to the Faraday cup (see Figure 32). It is held at a constant potential so that electrons will experience no force.

$G_s(u)$ is the inverse cumulative probability function

$$G_s(u) = \left(\frac{2}{\pi} \cdot \arctan \left(\sqrt{\tan \left(\frac{\pi}{2} \cdot X_{cs} \right) \cdot \tan \left(\frac{\pi}{2} \cdot u \right)} \right) \right)^{(1/n_s)}, \tag{38}$$

where n_s is a property of the material, and X_{cs} is calculated as

$$X_{cs} = \frac{X_c}{(0.9 + 1.1 \cdot X_c)}, \tag{39}$$

with

$$X_c = \frac{4 \cdot \left(B - e^{-E_{\text{trunc}}/A} \right)}{E_{\text{trunc}}}, \qquad E_{\text{trunc}} = \begin{cases} E_{\text{remain}} & \text{if } (E_{\text{remain}} \geq 1\text{eV}), \\ 1 & \text{otherwise,} \end{cases} \tag{40}$$

where A and B are parameters of the material.

The emission angle θ_{out} respect to the surface normal will be calculated by the cosine law [53]

$$\theta_{\text{out}} = \arcsin(\sqrt{u}), \tag{41}$$

and the azimuthal angle $\varphi \in [0, 2\pi[$ can be easily calculated by means of a uniform probability density as [53]

$$\varphi_{\text{out}} = 2\pi u, \tag{42}$$

where $u \in [0, 1]$ is a random number (evidently different each time that appears).

In the simulations we are going to use the parameters indicated in Table 2, which are typical values for copper.

Table 2: Values of the parameters used to calculate the emission energy: n_b, X_{cb}, and n_s have been extracted from [54], A and B from [55].

n_b	X_{cb}	n_s	A	B
1.5	0.9	0.51	4	5.8

Figure 31 shows the percentage of electrons of the dark currents (with respect to the output plane of the RF gun) that reach a certain axial distance in the drift tube considering or neglecting the SEY. Evidently, if the axial distance increases, the number of electrons decreases because some of them are absorbed when impact on the surface. We can see that the difference between the two cases is significant for short distances (less than 60 cm) and tends to decrease as the propagation distance increases. For distances between 5 and 10 cm, we find differences of around 12-14% between both curves. On the other hand, for an axial distance of 60 cm the differences are reduced to less than 1%. In conclusion, the approximation that all electrons that hit the drift tube are absorbed works very well at distances greater than 60 cm.

Now, we are going to optimize the design of the solenoid (whose dimensions are indicated in Figure 28) that allows maximizing the number of electrons detected by the Faraday cup. Figure 32 shows the scheme of the positions and dimensions of the Faraday cup and the solenoid coupled to the 1.6 cell RF gun. For this S-band photoinjector, we have that $r_{\text{out}} = 1.4$ cm. The dimensions of the Faraday cup are $L_{\text{cup}} = 3.03$ cm and $r_{\text{in}} = 0.609$ (to achieve a 50 Ω impedance matching). The axial position of the Faraday cup is fixed by the design provided by the INFN: $z_{\text{cup}} = 109.355$ cm.
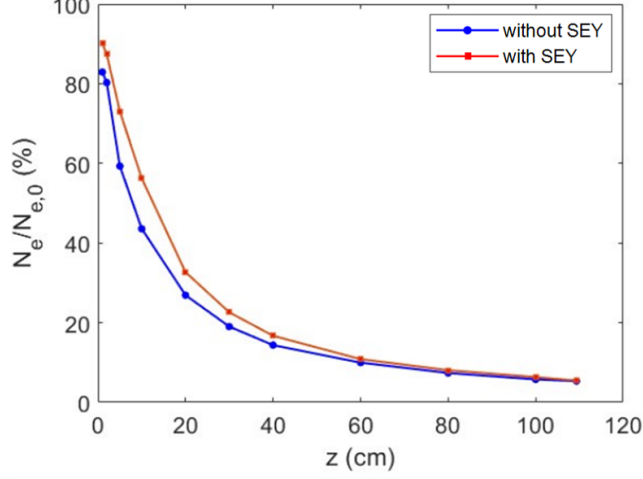
Figure 31: Comparison of the percentage of electrons (with respect to the initial value at the exit of the RF gun) reaching an axial distance z in the drift tube between the case with SEY and without SEY (considering that all electrons that hit the drift tube are absorbed).
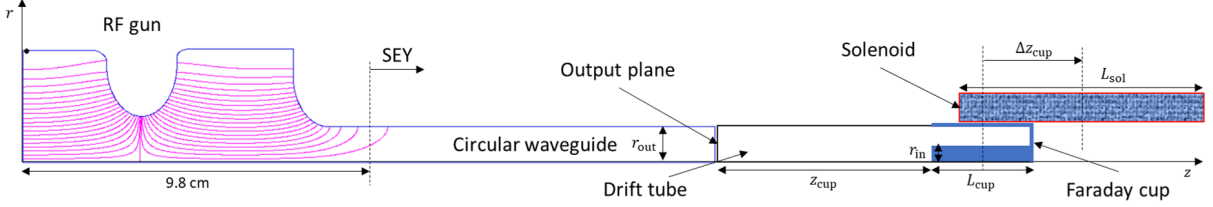

Figure 32: Scheme of the layout of the Faraday cup together with the solenoid to improve electron detection efficiency. Not to scale.

Thus, Figure 33 shows the percentage of electrons that are detected in the Faraday cup for different magnetic fields and positions of the solenoid. It can be seen that the presence of the solenoid significantly improves the amount of electrons detected by the Faraday cup. While without solenoid only 2.4% of the initial electrons are detected, with the solenoid up to 6.7% are detected for a magnetic field of 0.5 T and $\Delta z_{cup} = 7.5$ cm, which is therefore the optimum design of the solenoid. Nevertheless, the percentage of electrons detected in the Faraday cup is still very low ($< 7\%$) so the initial design provided by the INFN should be change (specifically z_{cup} should be shorter). If z_{cup} cannot be reduced in the real setup, another option may be to use the beam emittance compensating solenoid itself (remember that is turned off in the simulations) to focus the electrons instead of the additional solenoid that we have designed.
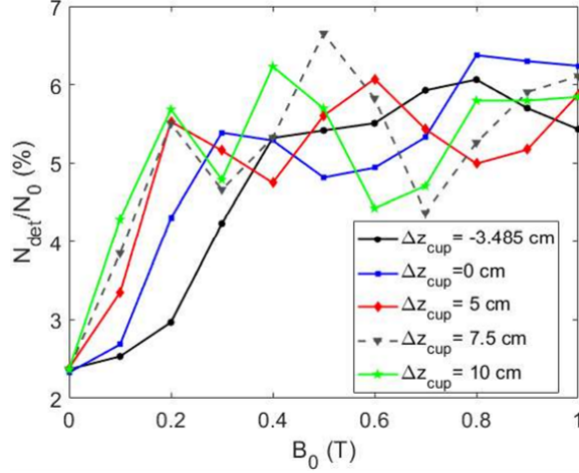
Figure 33: Percentage of electrons detected by the Faraday cup (normalised to the initial value at the output of the RF gun) as a function of the solenoid's magnetic field in its center B_0, for different axial positions of the solenoid. Δz_{cup} is the distance between the centers of the Faraday cup and the solenoid (see Figure 32).

3.1.3   5.6 cell RF electron gun injector

In this section we are going to simulate the dark current emission for an X-band 5.6 cell RF gun whose design has been proposed by D. González-Iglesias et al. [56] and meets the CompactLight project (XLS) [4] design study requirements. This RF gun is intended to operate at $f = 1/T_{\text{RF}} = 11.994$ GHz in the π-mode with a cathode gradient of 200 MV/m. Figure 34 shows the cross section of this RF gun, as well as the direction of the electric field. It consists of a photocathode, a coaxial coupler and six cells coupled by elliptical irises: a first cell with length 0.6 $\lambda/2$ and five cells with length $\lambda/2$. In the coaxial coupler, there is a region with $\varepsilon_{\text{r}} = \mu_{\text{r}} = 0.6 + 0.8i$ which represents a very lossy material with relative permittivity and permeability of ε_{r} and μ_{r} equal to unity $(0.6^2 + 0.8^2 = 1.0)$. If the length of the lossy dielectric is much longer than the absorption length in this dielectric, the forward running wave is completely absorbed and the line is terminated by a matched load. Consequently, this is a way to ensure that there will not be a reflected wave from the end of the waveguide that is filled with this *artificial* material, allowing a better calculation of the coupling factor between the RF gun and the coaxial coupler with SUPERFISH [57].
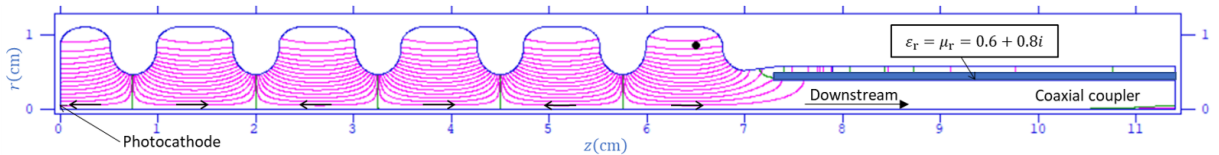

Figure 34: Cross section of the 5.6 cell RF gun with the coaxial coupler. The structure has symmetry of revolution around the z-axis. The field lines in the cavity are lines of constant rB_{φ}, which are parallel to the electric field.

The amplitude of the electric field along the gun axis is shown in Figure 35. We can see that the electric field is in phase opposition between cells, as it is expected for the π-mode. Otherwise, the surface electric field along the RF gun contour is shown in Figure 36. As in the 1.6 cell RF gun, the surface electric field is higher at the center of

the photocathode and at the irises, where the electron emission will be relevant.
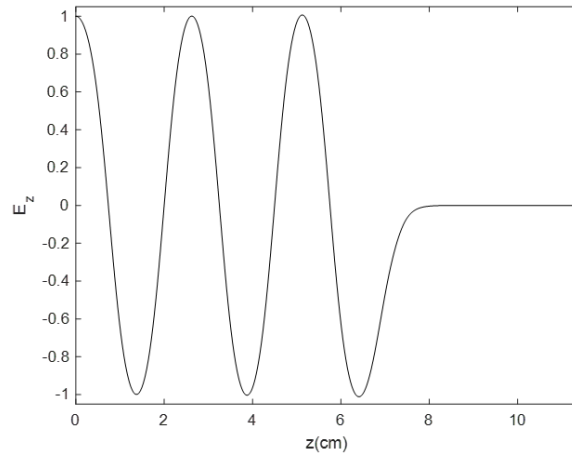

Figure 35: Electric field along the axis of the 5.6 cell RF gun, normalized to the maximum value at photocathode.
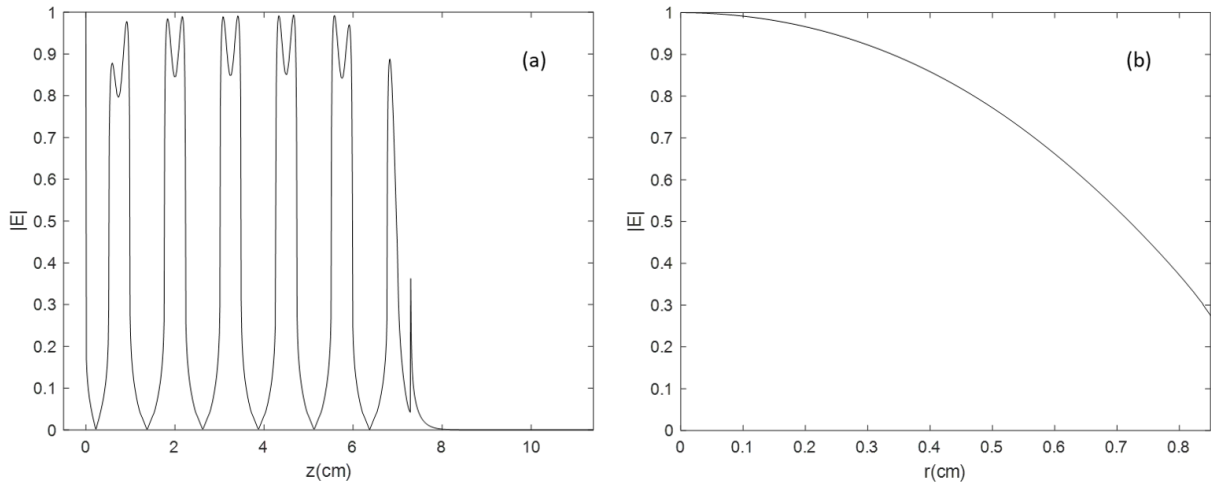

Figure 36: (a) Surface electric field as a function of the axial position. The last peak corresponds to the lossy material surface. (b) Electric field at the photocathode surface as a function of the radial position. Values normalized to the maximum value at photocathode of the 5.6 cell RF gun.

We are going to use the parameters indicated in Table 3 to perform the simulations in the 5.6 cell RF gun.

Table 3: Values of the field enhancement factor β, work function ϕ, density of emitters n and tip radius r_{em} used for the simulation of dark currents in the 5.6 cell RF gun.

β	$\phi(\mathrm{eV})$	$n\,(\mathrm{m}^{-2})$	$r_{\mathrm{em}}(\mu\mathrm{m})$
30	4.5	10^{6}	0.1

Figure 37 shows the positions of emitted macroparticles at different times. Due to the distribution of the electric field, dark currents are emitted periodically from the cathode, and second, fourth and sixth iris at $t = T_{\mathrm{RF}}/4$ and from the other irises at $t = 3T_{\mathrm{RF}}/4$.
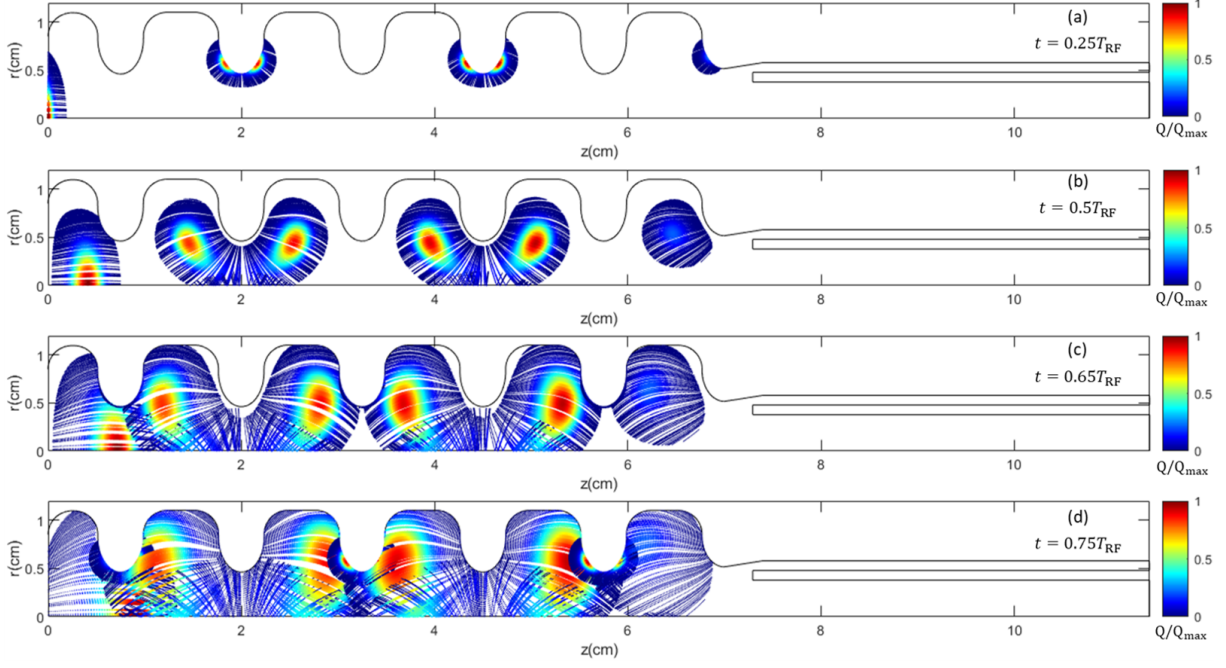
31

Figure 37: The dark current macroparticles positions (projected in the (r, z) plane) at the time instant (a) $t = 0.25T_{\mathrm{RF}}$, (b) $t = 0.5T_{\mathrm{RF}}$, (c) $t = 0.65T_{\mathrm{RF}}$ and (d) $t = 0.75T_{\mathrm{RF}}$. Color indicates the charge of the macroparticles normalised to the maximum macroparticle charge $Q_{\mathrm{max}} = -2781e$.

Figure 38: The dark current macroparticles positions (projected in the (r, z) plane) emitted from the fourth iris at the time instant (a) $t = 0.5T_{\mathrm{RF}}$, (b) $t = 1.5T_{\mathrm{RF}}$, (c) $t = 2.5T_{\mathrm{RF}}$ and (d) $t = 3.5T_{\mathrm{RF}}$. Color indicates the charge of the macroparticles normalise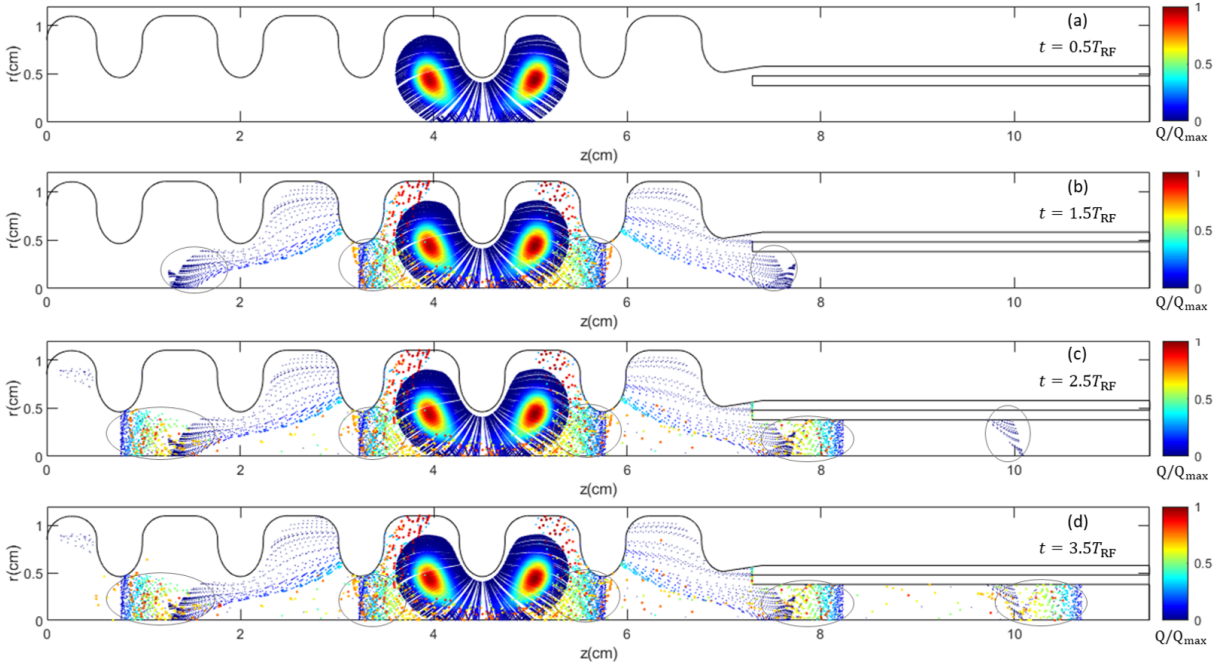d to the maximum macroparticle charge $Q_{\mathrm{max}} = -2630e$. Gray circles indicate the downstream and upstream bunches.

In Figure 39, we have plotted the emitted dark current and the different contributions (impact, downstream and upstream) as a function of time. Approximately 97.3% of emitted electrons impact on the surface of the structure and have kinetic energies > 10 keV. Approximately the 50% of these electrons hits the inner walls of the cells at rather small (less than 1 MeV) energy. Therefore, as in the previous case, secondary electron emission can be neglected. The downstream electrons that arrive to a distance of 7.5 cm from the cathode represent 0.7% of the emitted electrons while upstream electrons that impact on the photocathode are the 2%.
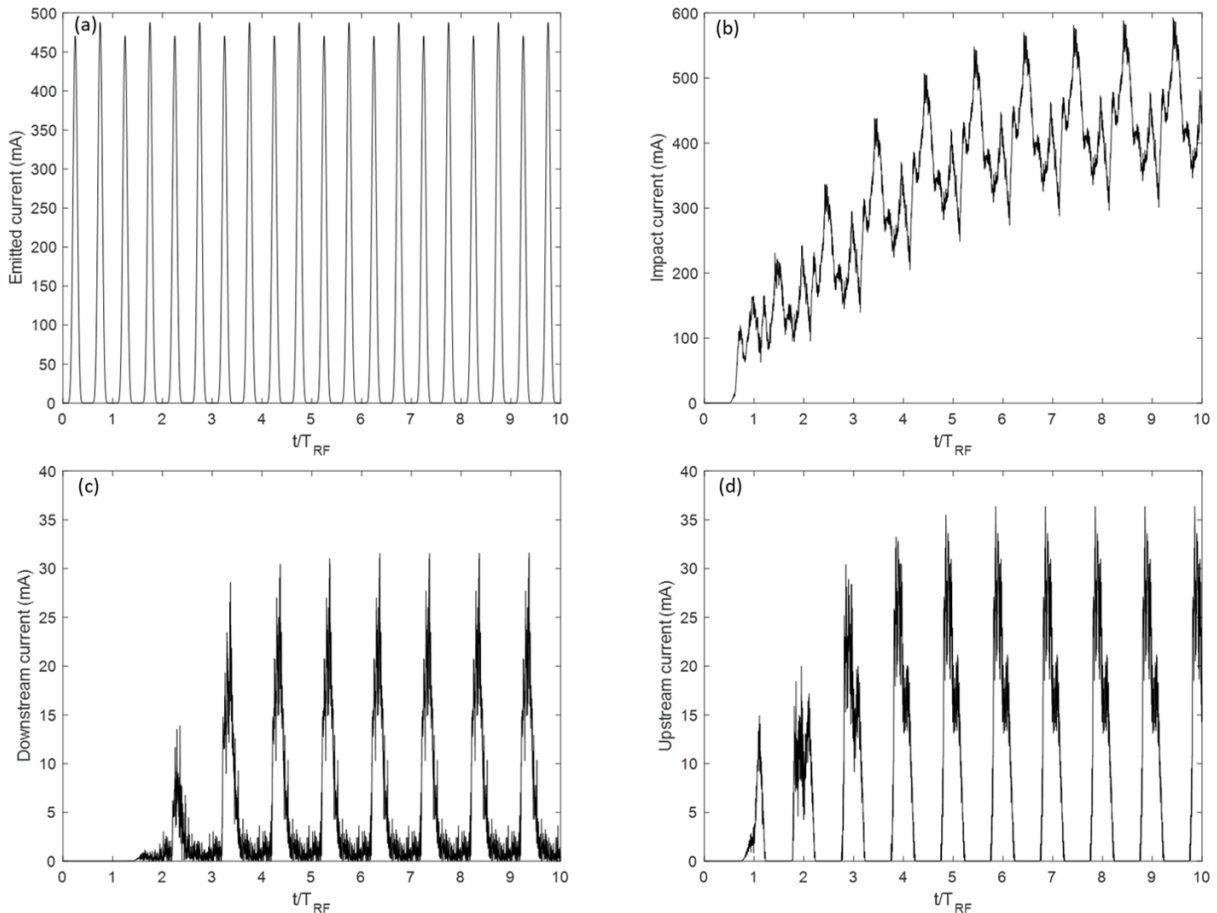

Figure 39: (a) Emitted dark current, (b) current that impacts on the surface of the structure, (c) downstream current that arrives to an axial distance of 7.5 cm from the cathode and (d) upstream current that arrives to the photocathode as a function of time.

In this case upstream and downstream electrons travel in bunches because they are coupled to the RF signal when passing a greater number of cells. For this reason, downstream and upstream currents have narrow peaks, as it can be seen in Figure 39c,d. To better visualize it, Figure 38 shows the positions of emitted macroparticles from the fourth iris at different periods. It can be seen that upstream and downstream electrons travel finally in bunches, which are indicated with gray circles. Consequently, in the kinetic energy spectra (Figure 40) we can see narrow peaks which correspond to the electrons that were emitted from different zones of the RF gun, which have been accelerated in a different number of cells.

33
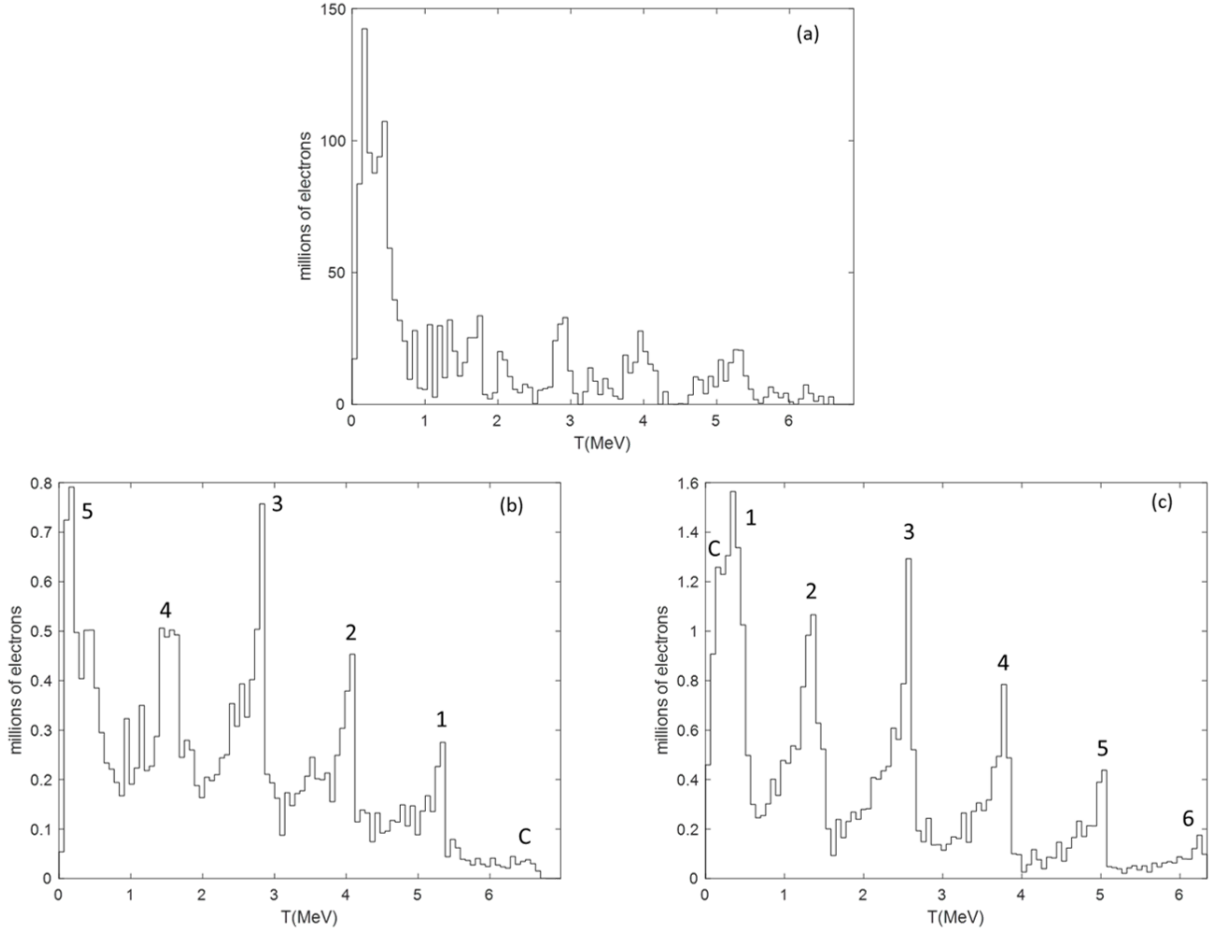
Figure 40: Kinetic energy spectra for (a) impact electrons, (b) downstream electrons and (c) upstream electrons after $10T_{\mathrm{RF}}$. We have indicated the number of the iris (C corresponds to the cathode) where electrons of the peak were mainly emitted from.

These results are qualitatively in concordance with recent results [58] obtained for a C-band RF gun using the 3D electromagnetic field analysis software package CST [59] to calculate the dark currents with a particle-in-cell (PIC) method to solve the electron dynamics taking into account the space charge.

3.2 Photomultiplier tubes

3.2.1 Design

A PMT has been designed in 2D with 8 box-and-grid dynodes with the voltage ratios indicated in Table 4. The structure can be seen in Figure 41. The outer rectangle simulates the metallic covering that surrounds the PMT and is connected to the supply voltage (the cathode voltage).
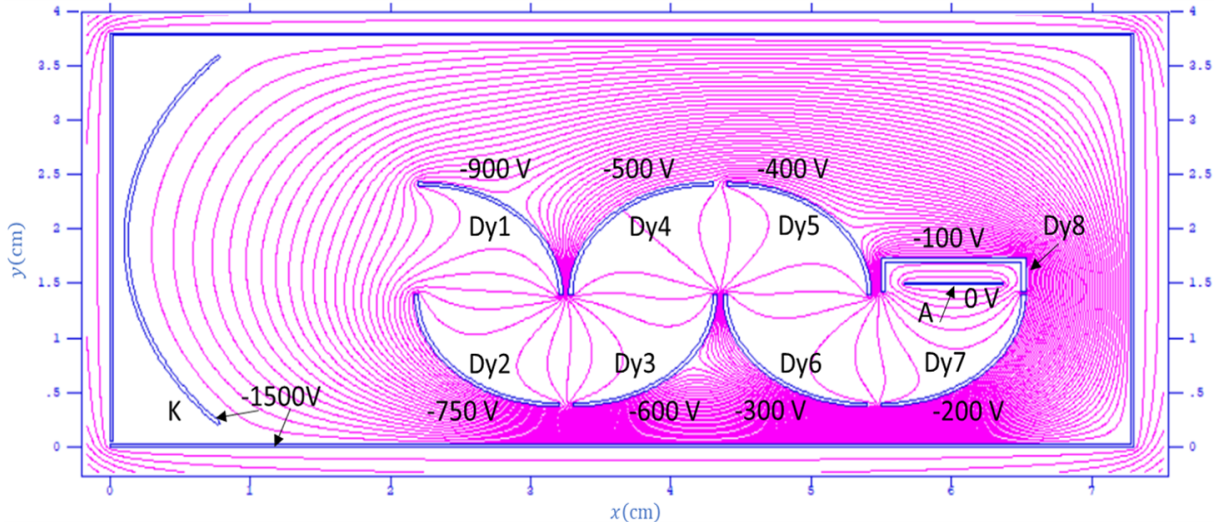

Figure 41: Designed 2D PMT structure consisting of a curved cathode (K) (radius 2.5 cm), 8 dynodes (Dy) and an anode (A). The equipotential lines and the voltages in the different corresponding elements are shown at a supply voltage of -1500 V. The electric field is perpendicular to the equipotential lines.

Table 4: Voltage ratios between the cathode (K), dynodes (Dy) and the anode (A).

Electrodes	K	Dy1	Dy2	Dy3	Dy4	Dy5	Dy6	Dy7	Dy8	A
Ratio	6	1.5	1.5	1	1	1	1	1	1	1

To calculate the total SEY of dynodes material, we will use the modified Vaughan's model with $\delta_{\text{low}} = k_E = k_\delta = 1, E_0 = 10$ eV, $E_{\text{max}} = 650$ eV, $\delta_{\text{max}} = 8.2$ and $k = 0.95$. Figure 42 shows a plot of the total SEY curve for those parameters and normal incidence.

The parameters have been chosen so that the SEY curve is as close as possible to the Cu-BeO-Cs SEY curve, which is a material that is often used to coat the dynodes, since it has a SEY quite high [40]. In Figure 43, a comparison is made of the SEY curve that we are simulating (Figure 42, but on a logarithmic scale) with the real curve of Cu-BeO-Cs so that the similarity of the curves can be seen.
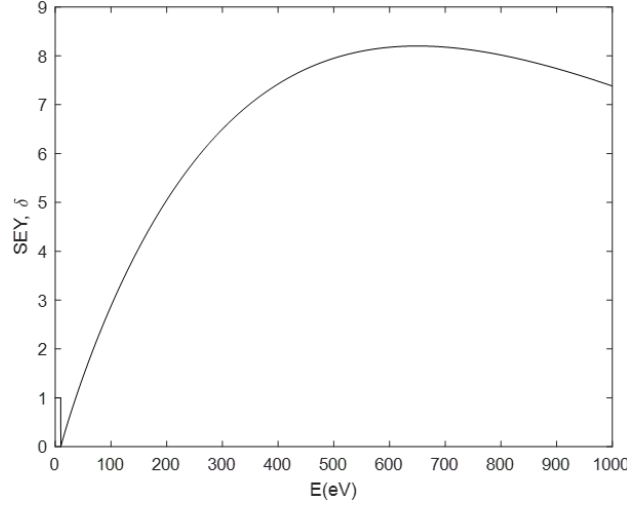
Figure 42: Modified Vaughan's total SEY curve for normal incidence and $\delta_{\text{low}} = k_E = k_\delta = 1$, $E_0 = 10$ eV, $E_{\text{max}} = 650$ eV, $\delta_{\text{max}} = 8.2$ and $k = 0.95$.
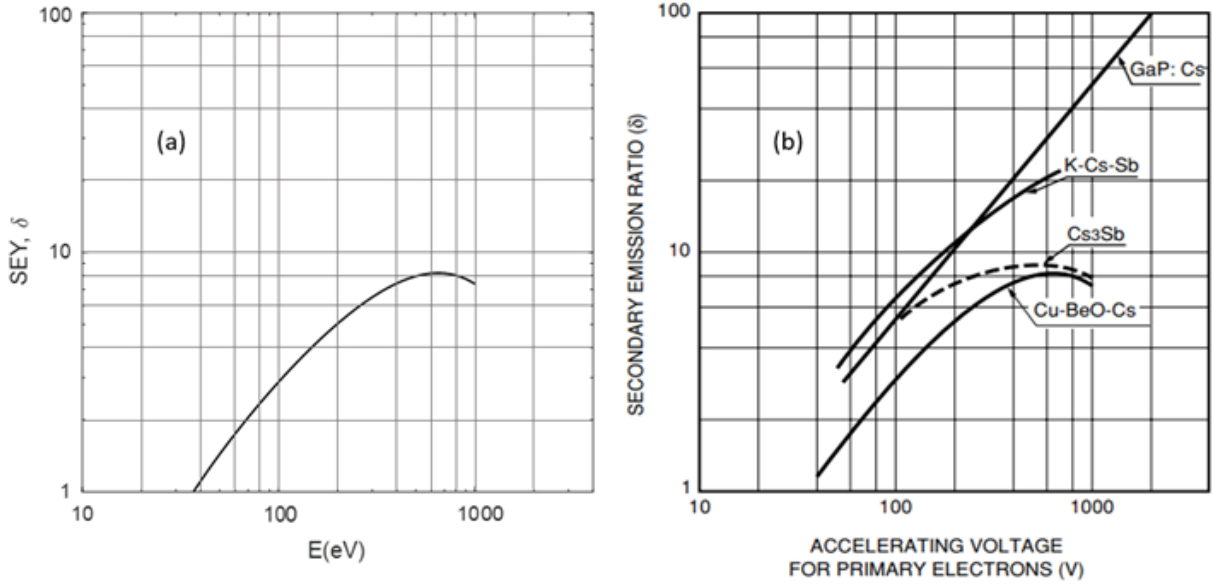

Figure 43: Comparison between (a) simulated SEY curve and (b) SEY curve for different secondary emissive materials which are typically used in dynodes [40].

3.2.2 Simulation program

The 2D electrostatic field is calculated with the software SUPERFISH that gives us the values in a 2D grid. For this reason, the fields in an arbitrary position (x, y) are calculated using a bilinear interpolation, equation (34). The electron dynamics has been solved using the Boris method with time steps of 4 ps and neglecting space charge effects. We will consider that the electrons are emitted without kinetic energy from the cathode. These electrons are accelerated towards the first dynode where they impact with enough energy to emit secondary electrons, which will accelerate towards the next dynode until they impact and more electrons are emitted. This process is repeated in the different dynodes until the electrons are collected at the anode, where an electric current will be measured. We will remove the electrons that do not enter in the electron multiplier and the (effective) electrons that escape from it through the slits between dynodes.

36

Thus, when an electron hits a dynode, if the impact kinetic energy is less than E_0 we will assume that the electrons are elastically reflected, while if $E > E_0$ a number $\delta(E, \theta)$ of electrons per incident electron will be emitted. However, we will use an effective electron model, so only a single macroparticle will be emitted with $\delta(E, \theta)$ times the number of electrons it had before impact. Therefore, an electron emitted from the cathode will arrive at the anode as an effective electron with a number of electrons

$$N = \prod_{j=1}^{J} \delta_j, \tag{43}$$

where J is the total number of collisions that the effective electron has undergone and δ_j is the SEY value corresponding to the j collision.

However, actually, the number of emitted electrons follows a Poisson distribution whose mean value is $\delta(E, \theta)$. For this reason, we have also calculated the number of secondary electrons emitted in this way. Thus, after j impacts the number of electrons of the effective electron is calculated as

$$N_{j+1} = \sum_{n=1}^{N_j} \text{Poisson}\left(\delta_j, u\right), \tag{44}$$

where N_j is the number of electrons that the macroparticle contained before the j impact, and $\text{Poisson}\left(\delta_j, u\right)$ is the random integer number of electrons emitted that has been calculated following a Poisson distribution with mean value δ_j with the aid of a random number $u \in [0, 1]$ (see Appendix B). We have not made the substitution $\delta_j \rightarrow \text{Poisson}\left(\delta_j, u\right)$ in equation (43) in order to avoid the disappearance of the macroparticle if $\text{Poisson}\left(\delta_j, u\right)$ gives 0. For this reason, the equation (44) calculates the contribution of each electron that is contained in the macroparticle before the j collision.

Regarding the kinetic energy of the macroparticle after a collision, on the one hand, we will assume that it is reflected elastically if the primary kinetic energy E satisfies $E < E_0$. On the other hand, true secondary electrons are emitted with a kinetic energy of a few eV, which does not depend on the primary electron conditions. Thus, if $E \geq E_0$, we will calculate the departure kinetic energy E_{out} as [33]

$$E_{\text{out}} = \sigma_E \sqrt{-2 \ln u}, \tag{45}$$

where $u \in [0, 1]$ is a random number and $\sigma_E = 2$ eV. This expression allows us to generate values for the departure kinetic energy following a Rayleigh probability distribution density (see Figure 44)

$$f(E_{\text{out}}) = \frac{E_{\text{out}}}{\sigma_E^2} \exp\left(-\frac{E_{\text{out}}^2}{2\sigma_E^2}\right), \tag{46}$$

where σ_E is the standard deviation value of the distribution. Note that the Rayleigh distribution is normalised, since

$$\int_0^\infty f(E_{\text{out}}) dE_{\text{out}} = 1. \tag{47}$$

The emission angle θ_{out} respect to the surface normal will be calculated by the cosine law, equation (41). However, as we are in a 2D-simulation, we only have two possibilities for the azimuthal angle: emission produced at an angle θ_{out} clockwise or counterclockwise

from normal. This choice can be done generating a new random number u and seeing if it is greater or less than 0.5.
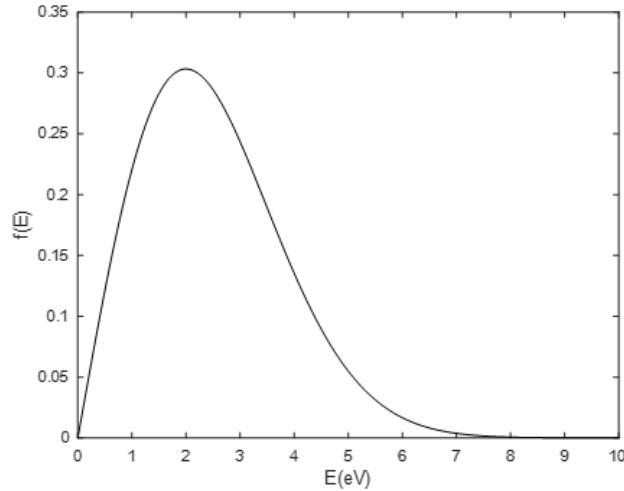

Figure 44: Rayleigh probability distribution density with $\sigma_E = 2$ eV.

We are going to carry out simulations to study the dependence of the gain, the electron transit time (ETT) and the transit time spread (TTS) with the magnetic field (in the z-direction) and the supply voltage.

Thus, we will emit a total of $N_T = 10000$ electrons (this value is enough to have sufficient statistics) from uniformly distributed positions on the cathode. We will calculate the gain, the ETT and the TTS with the expressions

$$\text{Gain} = \frac{\sum_{k=1}^{K} N_k}{N_T}, \tag{48}$$

$$\text{ETT} = \frac{\sum_{k=1}^{K} N_k t_k}{\sum_{k=1}^{K} N_k}, \tag{49}$$

$$\text{TTS} = \sqrt{\frac{\sum_{k=1}^{K} N_k \left(t_k - \text{ETT}\right)^2}{\sum_{k=1}^{K} N_k - 1}}, \tag{50}$$

where K is the number of effective electrons that are finally collected at the anode, N_k is the number of electrons contained in the k-th macroparticle (calculated using equation (43) or (44)) and t_k is the time that has elapsed since it was emitted until has reached the anode. Note that the gain is defined with respect to the electrons emitted from the cathode (i.e. we do not consider the quantum efficiency of the cathode photoemission or losses in the the scintillator crystal), and the definition of the TTS corresponds to the standard deviation of ETT.

3.2.3 Results

Firstly, Figure 45 shows a simulation of 15 electrons emitted from the cathode for a supply voltage of -1500 V and different values of the magnetic field. We can see that the existence of a magnetic field $|B_z| \geq 0.5$ mT reduces the number of macroparticles collected at the anode and the number of collisions of these effective electrons. This fact explains that the gain decreases considerably with the existence of a small magnetic field, as it can be seen in Figure 47. The gain maximum is obtained for $B_z = 0.2$ mT because for this magnetic field macroparticles usually impact on 7 dynodes while in the absence of magnetic field there are some macroparticles that impact on 5, 6 or 7 dynodes (see Figure 45c,d). Furthermore, it can be seen that the gain increases with the supply voltage (in absolute value), as it is expected, since the SEY value increases if the potential difference between dynodes is higher.
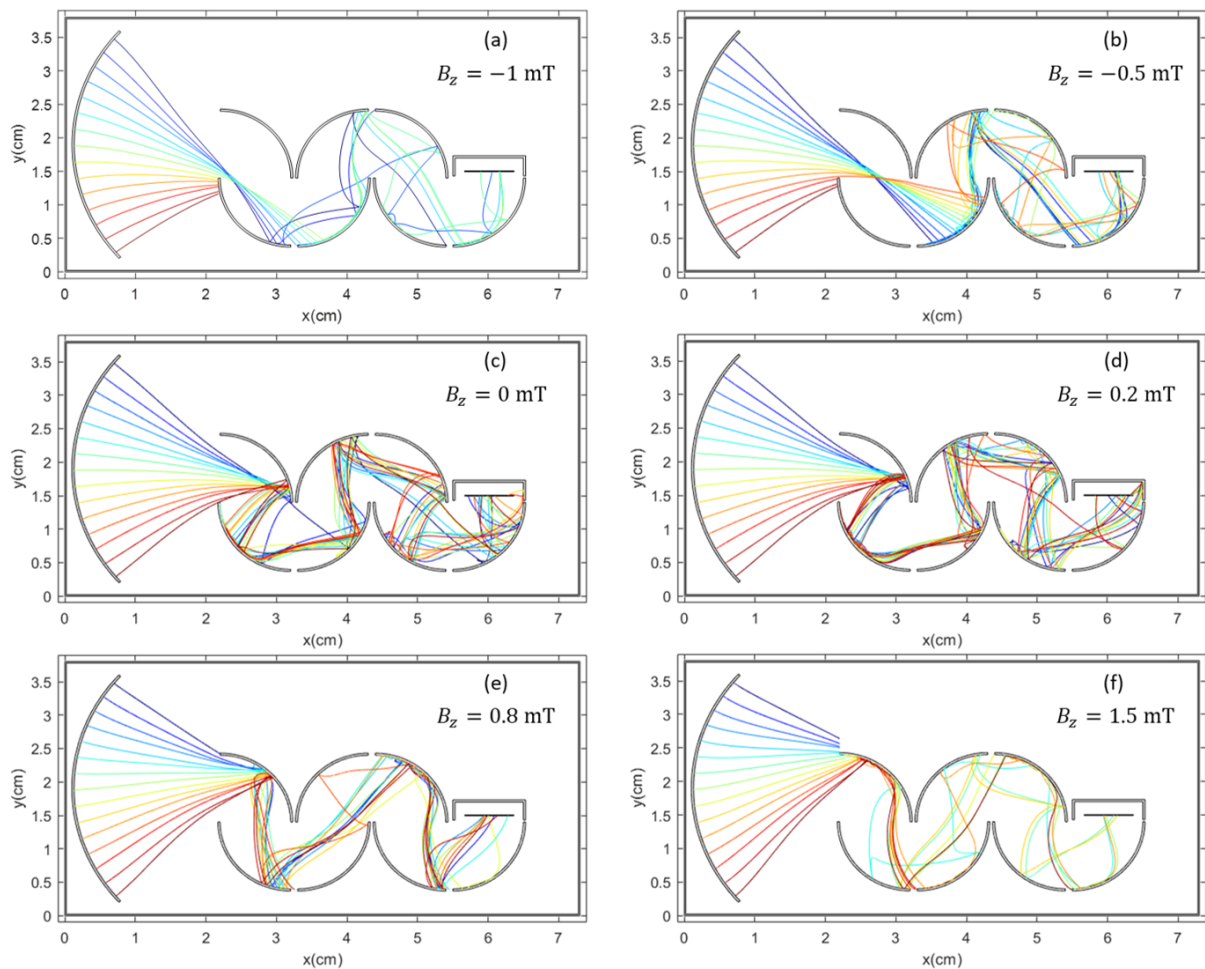

Figure 45: Trajectories followed by different macroparticles with a supply voltage of -1500 V and a magnetic field B_z of (a) -1 mT, (b) -0.5 mT, (c) 0 mT, (d) 0.2 mT, (e) 0.8 mT and (f) 1.5 mT.

On the other hand, it has been verified that both expressions (43) and (44) give us the same results for the gain, the ETT and the TTS (differences are always < 1% and are probably more influenced by the statistical variations than by using equation (43) or (44)). The only difference between the two methods of calculating the number of emitted electrons is obtained if we plot a histogram of the number of electrons contained in the

macroparticles that reach the anode (i.e the individual gain experienced by each effective electron), as it can be seen in Figure 46. If expression (43) is used, four peaks are seen due to the number of macroparticle impacts (4, 5, 6 or 7) on the dynodes (see Figure 45c) and the width is mainly due to variations in the SEY value because of the energy and the angle of impact. Otherwise, if expression (44) is used, there is a widening of the peaks due to statistical fluctuations in the random generation (following a Poisson distribution) of the integer number of emitted electrons. Therefore, this proves that the same results would have been obtained if we had taken into account a Poisson distribution to calculate the number of true secondary electrons emitted when we did the Faraday cup study in Section 3.1.2.
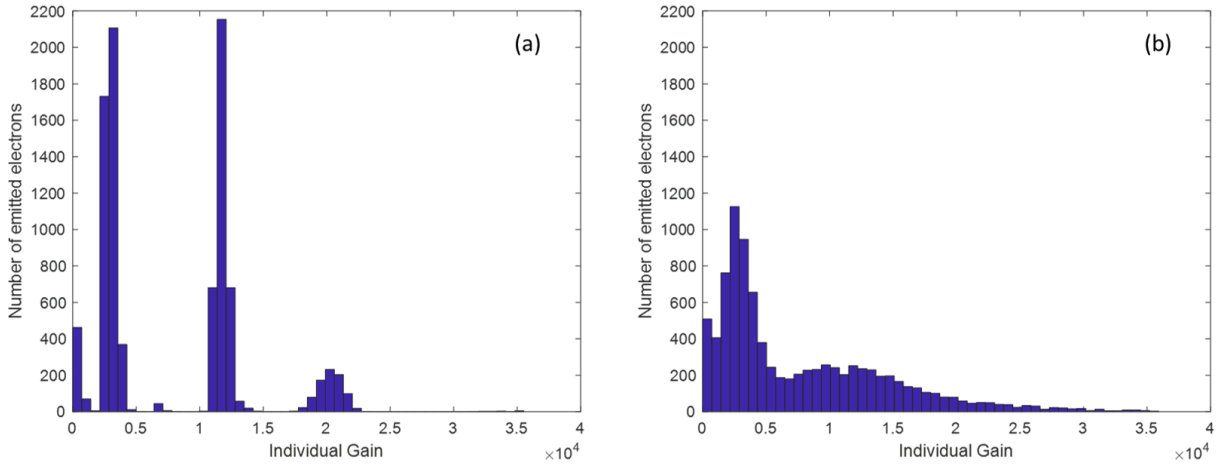

Figure 46: Histogram of the individual gain of the effective electrons arriving at the anode for a supply voltage of -1500 V and without magnetic field, calculating the number of emitted electrons following (a) equation (43) and (b) the Poisson distribution with equation (44).
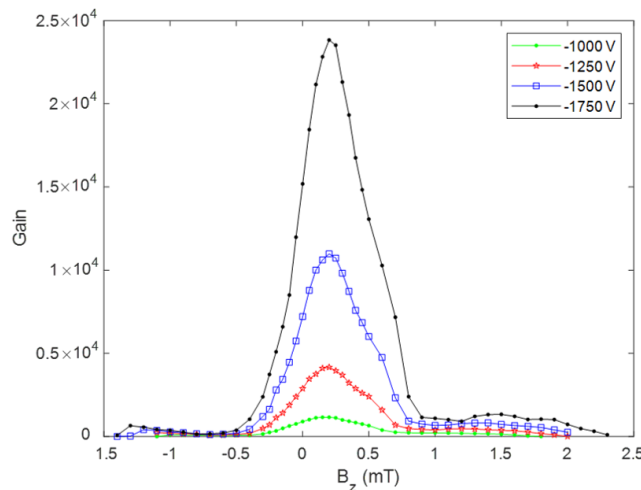

Figure 47: Gain as a function of the magnetic field (in the z-direction) for different supply voltages.

Regarding the ETT and the TTS, in Figure 48 it can be seen that they decrease if the supply voltage increases (in absolute value), as it is expected since the electric field is higher. Otherwise, we can see that the ETT and the TTS remain approximately constant for $B_z \in [0, 0.5]$ mT. If $B_z > 0.5$ mT or $B_z < 0$ mT, they decrease because macroparticles usually only impact on 4 dynodes (see Figure 45b,e) and therefore take less time for arriving to the anode. For higher values of the magnetic field the ETT and the TTS increase because macroparticles describe curved trajectories and take a longer time to reach the anode (see Figure 45a,f).
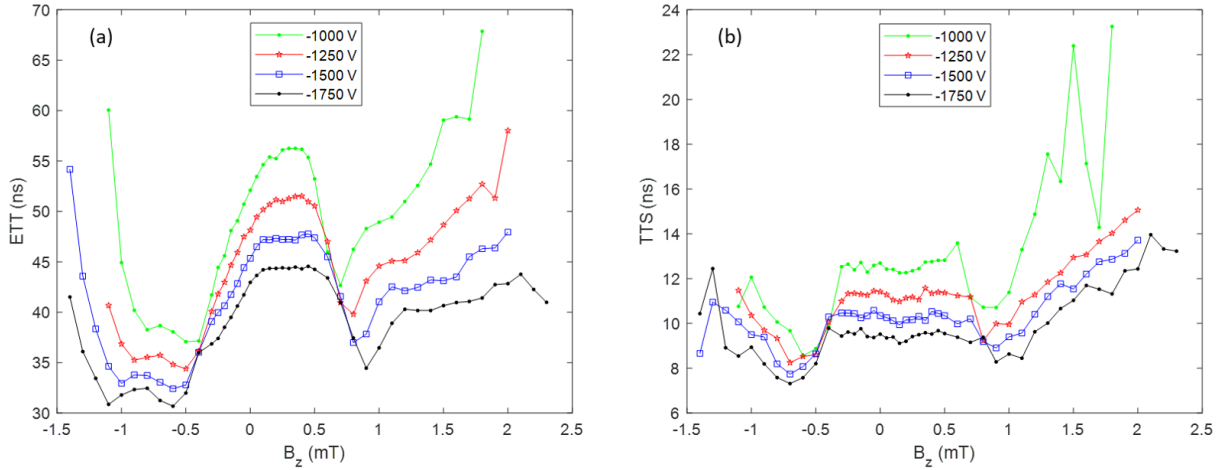

Figure 48: (a) ETT and (b) TTS as a function of the magnetic field (in the z-direction) for different supply voltages.

Hence, we have shown that the PMT is very sensitive to magnetic fields, which explains that even the Earth's magnetic field (0.025-0.065 mT) can influence the operation of a PMT.

41

4 Conclusions and future work

In this work we have studied the dark currents and the secondary electron emission in different devices. We can divide the results obtained in two main sections: the study of RF electron gun injectors and the study of a photomultiplier tube (PMT).

For the 1.6 cell and the 5.6 cell RF electron gun, we have programmed a code that calculates the dynamics of the dark currents using an effective electron model and neglecting space charge effects. We have shown that dark currents are mainly emitted from the photocathode and the irises because they have a higher surface electric field. Moreover, dark currents principally impact on the device surface with very high energies ($\sim$MeV) so is a good approximation to neglect the secondary electron emission. Kinetic energy spectra of upstream and downstream electrons have been plotted showing peaks corresponding to the number of accelerations that electrons undergo. These peaks are clearly visible for the 5.6 cell RF gun and are qualitatively similar to results published this year for a C-band RF structure [58]. As the S-band 1.6 cell RF electron gun has been recently built and experimental measurements will be taken soon at the INFN, we have also made an optimization of the setup in order to achieve the best detection of dark currents with a Faraday cup, proving that secondary electron emission is negligible if the Faraday cup is placed at a distance greater than 60 cm. We have designed a solenoid magnet that allows to increase the percentage of electrons that we can detect. However, this percentage is still very low so a better optimization is needed. The easiest way to achieve it is bringing near the Faraday cup, but its position depends on the experimental setup and maybe cannot be changed. For this reason, we are going to study if the beam emittance compensating solenoid itself (which is turned off in the simulations) can be used to focus the electrons in the inner cylinder of the Faraday cup instead of the additional solenoid that we have designed. Dark currents measurements will be very important in order to check the validity of our code optimising the different parameters of the simulations: the field enhancement factor β, the density of emitters n and the tip radius r_{em}. Moreover, we will try to incorporate space charge effects in our code.

For the PMT, we have designed a classical structure of a box-and-grid dynodes type. Using an effective electron model and the modified Vaughan's model for the secondary electron emission, we have simulated the dynamics of electrons. We have studied the dependence of the gain, the electron transit time (ETT) and the transit time spread (TTS) with the magnetic field and the supply voltage. As it is expected, in general, an increment of the voltage produces an increase in the gain and a decrease in the ETT and the TTS. In the case of the magnetic field, we have shown that even the Earth's magnetic field can modify the operation of a PMT. Therefore, magnetic fields can modify the measurements in a proton treatment room. In the future, it is intended to start a collaboration with Hamamatsu Photonics (a leading company in light technology and products, as PMTs), in order to simulate an accurate real structure of a PMT and compare our simulations with experimental measurements. As in the previous case, we will try to incorporate space charge effects in our simulation program.

A Generation of emitters with a uniform distribution in a surface with symmetry of revolution

The area of a body of revolution around the z-axis is given by the expression

$$S = \int_a^b 2\pi r(t) \sqrt{\left(\frac{dr}{dt}\right)^2 + \left(\frac{dz}{dt}\right)^2}\, dt = \int_a^b \sigma(t) dt, \tag{51}$$

where $r(t)$ and $z(t)$ are the continuously differentiable equations of the typical cylindrical coordinates $\{r, \varphi, z\}$ in terms of the parameter $t \in [a, b]$, and we have defined

$$\sigma(t) = 2\pi r(t) \sqrt{\left(\frac{dr}{dt}\right)^2 + \left(\frac{dz}{dt}\right)^2}, \tag{52}$$

which can be interpreted as a density of surface. Thus, we can generate points with a uniform distribution in this surface using three random real numbers $u_i \in [0,1] (i = 1, 2, 3)$. First, we calculate these two numbers:

$$t_r = a + u_1(b - a) \in [a, b], \tag{53}$$

$$\sigma_r = (\max \sigma) u_2 \in [0, \max \sigma]. \tag{54}$$

If $\sigma_r \leq \sigma(t_r)$ the point is accepted with the coordinates $r(t_r), z(t_r)$ and we calculate the azimuthal angle $\varphi = 2\pi u_3 \in [0, 2\pi]$.

In the extreme case where $r(z)$ is a vertical line (e.g. the photocathode), we have to generate emitters with a uniform distribution in a circle, which can be easily generated as $r = R\sqrt{u_1}$, where R is the radius of the circle, $\varphi = 2\pi u_3 \in [0, 2\pi]$ and $z = z_p$, where z_p is the plane that contains the circle.

B Generation of numbers with a Poisson distribution

The probability that n electrons are emitted from a surface is given by a Poisson distribution

$$P_n(\delta) = \frac{e^{-\delta} \cdot \delta^n}{n!}, \tag{55}$$

where $\delta \in \mathbb{R}^+$ is the distribution average (i.e. the SEY value) and is normalised since

$$\sum_{n=0}^{\infty} P_n(\delta) = 1. \tag{56}$$

Therefore, the Poisson cumulative probability function is

$$G(x, \delta) = \sum_{n=0}^{x} P_n(\delta), \quad x = 0, 1, 2..., \tag{57}$$

that satisfies $0 \leq G(x, \delta) \leq 1$. Hence, we can generate numbers following a Poisson distribution with the aid of a random number $u \in [0, 1]$ as

$$\text{Poisson}(\delta, u) = \begin{cases} 0 & \text{if } u \leqslant G(0, \delta), \\ N & \text{where } N \text{ satisfies } G(N - 1, \delta) < u \leqslant G(N, \delta). \end{cases} \tag{58}$$

References

[1] X-ray Optics. Accessed: July 2021.
URL `http://www.x-ray-optics.de/index.php/en/sources`

[2] F. Kiewiet, Generation of ultra-short, high brightness relativistic electron bunches, Ph.D. thesis, Applied Physics (2003). `doi:10.6100/IR571240`.

[3] E. Saldin, E. Schneidmiller, M. Yurkov, Coherence properties of the radiation from x-ray free electron laser, Optics Communications 281 (5) (2008) 1179–1188. `doi:https://doi.org/10.1016/j.optcom.2007.10.044`.

[4] XLS-CompactLight project. Accessed: July 2021.
URL `https://www.compactlight.eu/Main/HomePage`

[5] J. W. Wang, G. A. Loew, Field emission and RF breakdown in high gradient room temperature linac structures, in: Joint CERN-US-Japan Accelerator School: Course on Frontiers of Accelerator Technology: RF Engineering for Particle Accelerators, SLAC-PUB-7684, 1997.

[6] N. Shipman, Experimental study of DC vacuum breakdown and application to high-gradient accelerating structures for CLIC, Ph.D. thesis, The University of Manchester (August 2015).

[7] J. Norem, V. Wu, A. Moretti, M. Popovic, Z. Qian, L. Ducas, Y. Torun, N. Solomey, Dark current, breakdown, and magnetic field effects in a multicell, 805 MHz cavity, Phys. Rev. ST Accel. Beams 6 (2003) 072001. `doi:10.1103/PhysRevSTAB.6.072001`.

[8] P. Martínez-Reviriego, Numerical study of photocathode RF electron gun and dark currents with VSim, Master's thesis, Universitat de València (2020).

[9] R. R. Wilson, Radiological use of fast protons, Radiology 47 (5) (1946) 487–491. `doi:10.1148/47.5.487`.

[10] Particle Therapy Co-Operative Group, Manchester, U.K., Patient Statistics and Facilities Under Operation, 2019. Accessed: July 2021.
URL `https://www.ptcog.ch/index.php/patient-statistics`

[11] Particle Therapy Co-Operative Group, Manchester, U.K., Patient Statistics and Facilities Under Operation, 2021. Accessed: July 2021.
URL `https://www.ptcog.ch/index.php/facilities-in-operation`

[12] J. B. Farr, J. B. Flanz, A. Gerbershagen, M. F. Moyers, New horizons in particle therapy systems, Medical Physics 45 (11) (2018) e953–e983. `doi:https://doi.org/10.1002/mp.13193`.

[13] T. Bortfeld and J. Loeffler, Three ways to make proton therapy affordable, Nature 549 (2018) 451–453. `doi:10.1038/549451a`.

[14] X. Tian, K. Liu, Y. Hou, J. Cheng, and J. Zhang, The evolution of proton beam therapy: Current and future status (review), Molecular and Clinical Oncology 8 (1) (2018) 15–21. `doi:10.3892/mco.2017.1499`.

[15] F. Hueso-González, F. Fiedler, C. Golnik, T. Kormoll, G. Pausch, J. Petzoldt, K. E. Römer, W. Enghardt, Compton Camera and Prompt Gamma Ray Timing: Two Methods for In Vivo Range Assessment in Proton Therapy, Frontiers in Oncology 6 (2016) 80. `doi:10.3389/fonc.2016.00080`.

[16] J. M. Verburg, J. Seco, Proton range verification through prompt gamma-ray spectroscopy, Physics in Medicine and Biology 59 (23) (2014) 7089–7106. `doi:10.1088/0031-9155/59/23/7089`.

[17] C. Golnik, F. Hueso-González, A. Müller, P. Dendooven, W. Enghardt, F. Fiedler, T. Kormoll, K. Roemer, J. Petzoldt, A. Wagner, G. Pausch, Range assessment in particle therapy based on prompt-ray timing measurements, Physics in Medicine and Biology 59 (18) (2014) 5399–5422. `doi:10.1088/0031-9155/59/18/5399`.

[18] F. Hueso-González, T. Bortfeld, Compact Method for Proton Range Verification Based on Coaxial Prompt Gamma-Ray Monitoring: A Theoretical Study, IEEE Transactions on Radiation and Plasma Medical Sciences 4 (2) (2020) 170–183. `doi:10.1109/TRPMS.2019.2930362`.

[19] J. Smeets et al., Prompt gamma imaging with a slit camera for real-time range control in proton therapy, Physics in Medicine and Biology 57 (11) (2012) 3371–3405. `doi:10.1088/0031-9155/57/11/3371`.

[20] F. Hueso-González, M. Rabe, T. A. Ruggieri, T. Bortfeld, J. M. Verburg, A full-scale clinical prototype for proton range verification using prompt gamma-ray spectroscopy, Physics in Medicine & Biology 63 (18) (2018) 185019. `doi:10.1088/1361-6560/aad513`.

[21] M. Grodzicka-Kobylka, M. Moszyński, T. Szcześniak, Silicon photomultipliers in gamma spectroscopy with scintillators, Nuclear Instruments and Methods in Physics Research Section A: Accelerators, Spectrometers, Detectors and Associated Equipment 926 (2019) 129–147, silicon Photomultipliers: Technology, Characterisation and Applications. `doi:https://doi.org/10.1016/j.nima.2018.10.065`.

[22] J. Kim, M. Yoon, Design of a compact gantry for carbon-ion beam therapy, Phys. Rev. Accel. Beams 22 (2019) 101601. `doi:10.1103/PhysRevAccelBeams.22.101601`.

[23] B. Qin, R. Zhao, X. Liu, Q. Chen, H. Chen, K. Liu, J. Yang and D. Li, Comparison of beam optics for normal conducting and superconducting gantry beamlines applied to proton therapy, International Journal of Modern Physics A 34 (36) (2019) 1942015. `doi:10.1142/S0217751X19420156`.

[24] O. Richardson, LI. Some applications of the electron theory of matter, The London, Edinburgh, and Dublin Philosophical Magazine and Journal of Science 23 (136) (1912) 594–627. `doi:10.1080/14786440408637250`.

[25] W. Schottky, Über den Einfluss von Strukturwirkungen, besonders der Thomsonschen Bildkraft, auf die Elektronenemission der Metalle, Physik. Zeitschr 15 (1914) 872–878.

[26] M. von Laue, Jb. Radioakt. u. Elektr. 15 (1914) 205, 257, 301.

[27] S. Dushman, Electron emission from metals as a function of temperature, Phys. Rev. 21 (1923) 623–636. `doi:10.1103/PhysRev.21.623`.

[28] R. H. Fowler, L. Nordheim, Electron emission in intense electric fields, Proceedings of the Royal Society of London. Series A, Containing Papers of a Mathematical and Physical Character 119 (781) (1928) 173–181.
URL `http://www.jstor.org/stable/95023`

[29] L. Nordheim, The effect of the image force on the emission and reflexion of electrons by metals, Proceedings of the Royal Society of London. Series A, Containing Papers of a Mathematical and Physical Character 121 (781) (1928) 626–639.
URL `http://doi.org/10.1098/rspa.1928.0222`

[30] E. L. Murphy, R. H. Good, Thermionic emission, field emission, and the transition region, Phys. Rev. 102 (1956) 1464–1473. `doi:10.1103/PhysRev.102.1464`.

[31] Potential energy electron in metal. Accessed: July 2021.
URL `http://5579319.s21i.faiusr.com/2/ABUIABACGAAg1uXRqgUo8YyggAcwkAM4xwE.jpg`.

[32] R. H. Good, E. W. Müller, Field Emission, Springer Berlin Heidelberg, Berlin, Heidelberg, 1956, pp. 176–231. `doi:10.1007/978-3-642-45844-6_2`.

[33] D. González-Iglesias, Analysis of the multipactor effect in microwave waveguides and transmission lines, Ph.D. thesis, Universitat de València (May 2017).

[34] J. Vaughan, A new formula for secondary emission yield, IEEE Transactions on Electron Devices 36 (9) (1989) 1963–1967. `doi:10.1109/16.34278`.

[35] C. Vicente, M. Mattes, D. Wolk, B. Mottet, H. Hartnagel, J. Mosig, D. Raboso, Multipactor breakdown prediction in rectangular waveguide based components, in: IEEE MTT-S International Microwave Symposium Digest, 2005., 2005, pp. 1055–1058. `doi:10.1109/MWSYM.2005.1516852`.

[36] M. A. Furman, M. T. F. Pivi, Probabilistic model for the simulation of secondary electron emission, Phys. Rev. ST Accel. Beams 5 (2002) 124404. `doi:10.1103/PhysRevSTAB.5.124404`.

[37] J. de Lara, F. Perez, M. Alfonseca, L. Galan, I. Montero, E. Roman, D. Garcia-Baquero, Multipactor prediction for on-board spacecraft rf equipment with the mest software tool, IEEE Transactions on Plasma Science 34 (2) (2006) 476–484. `doi:10.1109/TPS.2006.872450`.

[38] R.L. Sheffield, E.R. Gray, J.S. Fraser, A new high-brightness electron injector for free-electron lasers driven by RF linacs, Nuclear Instruments and Methods in physics research A 250 (1-2) (1986) 71–76.

[39] David H. Dowell, Sources of Emittance in RF Photocathode Injectors: Intrinsic emittance, space charge forces due to non-uniformities, RF and solenoid effect, Tech. rep., SLAC, SLAC-PUB-16895, 1999.

[40] Hamamatsu Photonics K. K., Photomultiplier tubes. Basics ans applications, 4th Edition, 2017.
URL https://www.hamamatsu.com/resources/pdf/etd/PMT_handbook_v4E.pdf

[41] Enrique Muñoz Albaladejo, Development of a reconfigurable multi-plane compton telescope for hadrontherapy dose monitoring, Ph.D. thesis, Universitat de València (September 2019).

[42] Glenn F. Knoll, Radiation Detection and Measurement, 4th Edition, John Wiley and Sons, 2010.

[43] University of Chicago: Large-Area Picosecond Photo-Detectors Project. Accessed: July 2021.
URL https://psec.uchicago.edu/library/photomultipliers/Photonis_PMT_basics.pdf

[44] J. P. Boris, in: Proc. Fourth Conf. Numerical Simulations of Plasmas (Washington, D.C.: Naval Research Laboratory), 3, 1970.

[45] B. Ripperda, F. Bacchini, J. Teunissen, C. Xia, O. Porth, L. Sironi, G. Lapenta, R. Keppens, A comprehensive comparison of relativistic particle integrators, The Astrophysical Journal Supplement Series 235 (1) (2018) 21. doi:10.3847/1538-4365/aab114.

[46] K. Halbach, R. F. Holsinger, Superfish -A computer program for evaluation of RF cavities with cylindrical symmetry, Part. Accel. 7 (1976) 213–222.

[47] W. H. Press, S. A. Teukolsky, W. T. Vetterling and B. P. Flannery, Numerical recipes in C: the art of scientific computing, 2nd Edition, Cambridge University Press, 1997.

[48] R. A. Marsh, F. Albert, S. G. Anderson, G. Beer, T. S. Chu, R. R. Cross, G. A. Deis, C. A. Ebbers, D. J. Gibson, T. L. Houck, F. V. Hartemann, C. P. J. Barty, A. Candel, E. N. Jongewaard, Z. Li, C. Limborg-Deprey, A. E. Vlieks, F. Wang, J. W. Wang, F. Zhou, C. Adolphsen, T. O. Raubenheimer, Modeling and design of an X-band RF photoinjector, Phys. Rev. ST Accel. Beams 15 (2012) 102001. doi:10.1103/PhysRevSTAB.15.102001.

[49] K. L. Brown, G. W. Tautfest, Faraday-cup monitors for high-energy electron beams, Review of Scientific Instruments 27 (9) (1956) 696–702. doi:10.1063/1.1715674.

[50] Gerard Andonian and Pedro Frigola, Low Energy Faraday Cup, FARC-02-300, Revised July 11, 2007.
URL http://www.radiabeam.com/upload/1310534331FARC-02-300-ext.pdf

[51] V. Kumar, Understanding the focusing of charged particle beams in a solenoid magnetic field, American Journal of Physics 77 (2009) 737–741.

[52] RadiaBeam Technologies: Faraday Cups.
URL http://www.radiabeam.com/upload/catalog/pdf/14272334342015-03-24_faraday-cups.pdf

[53] J. Greenwood, The correct and incorrect generation of a cosine distribution of scattered particles for monte-carlo modelling of vacuum systems, Vacuum 67 (2) (2002) 217–222. `doi:https://doi.org/10.1016/S0042-207X(02)00173-2`.

[54] D. Wolk, J. Damaschke, C. Vicente, B. Mottet, H. Hartnagel, L. Galán, I. Montero, E. Román, M. Alfonseca, J. de Lara, D. Raboso, Surface treatments and coatings for reduction of multipactor and Passive InterModulation (PIM) effect in RF components, in: 4th International Workshop on Multipactor, Corona and Passive Intermodulation in Space RF Hardware. MULCOPIM 2003, 2003.
URL `http://hdl.handle.net/10486/663830`

[55] F. Pérez, J. de Lara, L. Conde, M. Alfonseca, L. Galán, D. Raboso, CEST and MEST: Tools for the simulation of radio frequency electric discharges in waveguides, Simulation Modelling Practice and Theory 16 (9) (2008) 1438–1452. `doi:https://doi.org/10.1016/j.simpat.2008.08.002`.

[56] D. González-Iglesias, A. Aksoy, D. Esperante, B. Gimeno, A. Latina, M. Boronat, C. Blanch, N. Fuster-Martínez, P. Martinez-Reviriego, P. Martín-Luna and J. Fuster, X-band RF photoinjector design for the CompactLight project, Sent for publication in Nuclear Inst. and Methods in Physics Research, A.

[57] James H. Billen and Lloyd M. Young, Poisson Superfish manual, LA-UR-96-1834, Revised January 13, 2006.

[58] V. Chernysh, A. Ermakov, A. Ieshkin, D. Kireev, V. Khankin, L. Ovchinnikova, V. Shvedunov, A. Tatarintsev, D. Yurov, Dark current issues for high gradient C-band medical linac, Journal of Instrumentation 16 (02) (2021) T02007. `doi:10.1088/1748-0221/16/02/t02007`.

[59] CST Studio Suite: 3D Electromagnetic field simulation software. Accessed: July 2021.
URL `https://www.cst.com`